

# Radio- $\gamma$ -ray response in blazars as a signature of adiabatic blob expansion

A. Tramacere, V. Sliusar, R. Walter, J. Jurysek, and M. Balbo

Department of Astronomy, University of Geneva, Chemin Pegasi 51, CH-1290 Versoix, Switzerland

Received August 11, 2021; accepted December 6, 2021

## ABSTRACT

*Context.* Multi-wavelength light curves in long-term campaigns show that, for several blazars, the radio emission occurs with a significant delay with respect to the  $\gamma$ -ray band, with timescales ranging from weeks to years. Such observational evidence has long been a matter of debate, and is usually interpreted as a signature of the  $\gamma$ -ray emission originating upstream in the jet, with the emitting region becoming radio transparent at larger scales.

*Aims.* In this paper, we show, by means of self-consistent numerical modelling, that the adiabatic expansion of a relativistic blob can explain these delays, reproducing lags compatible with the observed timescales.

*Methods.* We use the JetSeT framework to reproduce the numerical modelling of the radiative and accelerative processes, reproducing the temporal evolution of a single blob, from the initial flaring activity and the subsequent expansion. We follow the spectral evolution and the corresponding light curves, investigating the relations among the observed parameters, rise time, delay, and decay time, and we identify the link with physical parameters.

*Results.* We find that, when adiabatic expansion is active, lags due to the shift of the synchrotron frequency occur. The corresponding time lags have an offset equal to the distance in time between the flaring onset and the beginning of the expansion, whilst the rising and decaying timescales depend on the velocity of the expansion and on the time required for the source to exhibit a synchrotron self-absorption frequency below the relevant radio spectral window. We derive an inter-band response function, embedding the aforementioned parameters, and we investigate the effects of the competitions between radiative and adiabatic cooling timescales on the response. We apply the response function to long-term radio and  $\gamma$ -ray light curves of Mrk 421, Mrk 501, and 3C 273, finding satisfactory agreement on the log-term behaviour, and we use a Monte Carlo Markov Chain approach to estimate some relevant physical parameters. We discuss applications of the presented analysis to polarization measurements and to jet collimation profile kinematics. The collimation profiles observed in radio images are in agreement with the prediction from our model.

## 1. Introduction

In the unified scenario of the active galactic nuclei (AGN), blazars are understood as sources in which a relativistic jet is produced by the central engine and points close to our line of sight (Blandford & Rees 1978). Blazars are comprised of two kinds of AGN: BL Lacs and flat-spectrum radio quasars (FSRQs). BL Lac objects are marked by featureless optical spectra, while FSRQs show broad emission lines from hot high-velocity gas presumably located deep in the gravitational well of the central black hole. In a few cases, FSRQs show the presence of a blue ‘bump’ (Brown et al. 1989; Pian et al. 1999). Both BL Lacs and FSRQs show high flux from the radio to the  $\gamma$ -ray band, strong variability (Ulrich et al. 1997), and high polarisation observed in the optical band. Their spectral energy distributions (SEDs) show two main components: a low-energy component with power peaking in the range from the IR to the X-ray band, and a high-energy component peaking in the  $\gamma$ -rays. In the most widely accepted scenario, the low-energy component is understood as synchrotron (S) radiation emitted by ultrarelativistic electrons, and the high-energy bump is interpreted as inverse Compton (IC) emission for the case of a purely leptonic scenario (Blandford & Königl 1979) or dominated by high-energy emission of ultrarelativistic protons in the case of hadronic models (Böttcher et al. 2013). Despite the general consensus on this scenario, several open questions remain as to their puzzling behaviour that challenge our understanding of their observed phenomenology. In particular, long-term multiwavelength campaigns for several blazars have shown radio emission occurring

with a significant delay with respect to the  $\gamma$ -ray band, with timescales ranging from weeks to years (Pushkarev et al. 2010; Max-Moerbeck et al. 2014). This observational evidence is not compatible with different cooling timescales, and has been a matter of debate for several years. A possible interpretation was proposed by taking into account the different distances of the  $\gamma$ -ray and radio transparent region, with the moving region becoming transparent to the  $\gamma$ -rays (Blandford & Levinson 1995) and later to the radio frequencies (Blandford & Königl 1979). Delays between the GeV and radio variability of blazars have already been reported several times. Max-Moerbeck et al. (2014) found hints for GeV leading the radio in four blazars. In the case of Mrk 421, a delay of 40 days was reported in agreement with Hovatta et al. (2015). A much longer delay of  $140 \pm 20$  days was found by Esposito et al. (2015) in 3C 273 with a response decaying in  $\sim 190$  days. Finally, Rani et al. (2014) reported a delay of 82 days between the GeV and radio light curves of S5 0716+714 with a correlated change of the VLBI jet position angle and suggested that a shock in the jet first affected the gamma-ray emission and later triggered morphology shifts in the radio core. A key aspect to investigate in this scenario is to understand the role of the adiabatic expansion of the emitting region, and the consequences in terms of variation of the synchrotron self-absorption frequency (SSA), as presented in the seminal works by McCray (1969) and van der Laan (1969) and more recently Boula et al. (2018), Potter (2018), and Boula, S. & Mastichiadis, A. (2022). A recent analysis by Zacharias (2021) investigates the adiabatic expansion scenario, but focuses on the impact of the expansion

on the usual ‘double-humped’ SED shape rather than on the possible relation with the radio– $\gamma$  delay.

In this paper, we derive phenomenological trends linking the relevant timescales of the delay to the physical parameters of the emitting region, and we verify them by means of a self-consistent numerical modelling. We propose a response function based on the relevant phenomenological timescales that is able to reproduce the radio-delayed light curve as a response to the  $\gamma$ -ray, and we validate the phenomenological trends against the numerical simulations, investigating biases due to the competition between radiative and adiabatic cooling timescales. We apply this response to Mrk 421, Mrk 501, and 3C237, and obtain good agreement with the long-term radio trends. Finally, we employ a Monte Carlo Markov Chain (MCMC) approach to estimate physical parameters from the comparison between the response function convolution parameters and the prediction from the phenomenological trends. The paper is organised as follows. In section 2 we derive the phenomenological trends expected under the hypothesis of a moving blob expanding with uniform velocity, and we characterise the delay in terms of the velocity of expansion and of the consequent evolution of the SSA, finding a physical link between observed rise and decay timescales and the physical parameters of the blob and jet. In section 3.1, we describe our setup of numerical simulations done with the `JetSeT` code (Tramacere 2020; Tramacere et al. 2011; Tramacere et al. 2009), taking into account radiative, accelerative processes, and adiabatic expansion. The simulations reproduce the long-term temporal evolution of a single blob, from the initial flaring activity, and the subsequent expansion. In section 4 we compare the results for the cases of an expanding versus a non-expanding blob. In section 5 we follow the spectral evolution and the corresponding light curves for different values of the expansion velocity and for different radio frequencies. We propose a response function—embedding the relevant observed timescales—able to reproduce the radio light curve as a convolution with the  $\gamma$ -ray one, and we validate the phenomenological trends against the numerical simulations, studying the biases on the timescales embedded in the response functions resulting from competition between radiative and adiabatic cooling timescales. In section 6 we apply our model to observed data for Mrk 421, Mrk 501, and 3C 273, and we reproduce long-term radio light curves as convolution of the  $\gamma$ -ray light curve with the proposed response function. In section 7 we employ a MCMC approach to estimate physical parameters of the jet from a comparison between the response function convolution parameters and the prediction from the phenomenological trends. More specifically, we investigate estimates of the source size, the magnetic field index, the initial SSA frequency, the expansion velocity, and the spectral index of the electron distribution. We also compare our results with similar works in the literature, and discuss some implications of our model regarding the impact on the Compton dominance, hadronic models, and polarisation, and we also speculate on other possible causes of the delays, such as jet bending and the connection to the jet profile observed in the VLBI radio analysis. In section 8 we summarise our findings and discuss our upcoming extension of the presented model. In section A we provide instructions to reproduce the analysis and the numerical modelling presented in this paper.

## 2. Phenomenological setup of an expanding blob and synchrotron self-absorption

We assume that a spherical blob, characterised by an initial radius  $R_0$  and magnetic field  $B_0$  expands with a constant velocity

$\beta_{\text{exp}} = v_{\text{exp}}/c$ , and that the expansion begins at a time  $t_{\text{exp}}$ . All the quantities are measured in the frame of the emitting blob. Quantities expressed in the observer frame are labelled by the *obs* flag. The size of the blob can be expressed as

$$R(t) = R_0 + \beta_{\text{exp}} c (t - t_{\text{exp}}) H(t - t_{\text{exp}}), \quad (1)$$

where  $H$  is the Heaviside step function.

The time-dependent law of the magnetic field, dictated by flux freezing (Begelman et al. 1984) and energy conservation, reads

$$B(t) = B_0 \left( \frac{R_0}{R(t)} \right)^{m_B}, \quad (2)$$

where the index  $m_B \in [1, 2]$  depends on the geometric configuration of the magnetic field, with  $m_B = 2$  for a fully poloidal configuration, and  $m_B = 1$  for a fully toroidal configuration (Begelman et al. 1984). The adiabatic cooling will read (Longair 2010)

$$\dot{\gamma}_{\text{ad}}(t) = \frac{1}{3} \frac{\dot{V}}{V} \gamma = \frac{\dot{R}(t)}{R(t)} \gamma = \frac{\beta_{\text{exp}} c}{R(t)} \gamma, \quad (3)$$

where  $\gamma$  is the Lorentz factor of the electrons, and  $V$  is the volume of the region that we assume to be spherical. The corresponding cooling time can be expressed as

$$t_{\text{cooling}}^{\text{ad}}(t) = \frac{\gamma}{\dot{\gamma}} = \frac{R(t)}{\beta_{\text{exp}} c} = \frac{R_0 + \beta_{\text{exp}} c (t - t_{\text{exp}}) H(t - t_{\text{exp}})}{\beta_{\text{exp}} c}. \quad (4)$$

The evolution of the synchrotron self-absorption frequency can be expressed as (Rybicki & Lightman 1986)

$$\nu_{\text{SSA}}(t) = \nu_L(t) \left[ \frac{\pi \sqrt{\pi} e R(t) N(t)}{4 B(t)} f_k(p) \right]^{\frac{2}{p+4}}, \quad (5)$$

where  $e$  is the electron charge,  $N(t)$  is the particle number density at time  $t$ ,  $p$  is the power-law index of the electron distribution at the Lorentz factor most contributing to  $\nu_{\text{SSA}}(t)$ , and  $\nu_L(t) = \frac{e B(t)}{2\pi m_e c}$  is the Larmor frequency. The functions  $f_k(p)$  are approximated to percent accuracy as reported in Ghisellini (2013). Assuming that particles are confined ( $R^3 N(t) = N^{\text{tot}}$ ), and plugging Equation 2 and 1 into Equation 5 we obtain

$$\nu_{\text{SSA}}(t) \propto \left[ B(t)^{\frac{p+2}{2}} \frac{N^{\text{tot}}}{R(t)^2} \right]^{\frac{2}{p+4}}. \quad (6)$$

Setting the initial self-absorption frequency  $\nu_{\text{SSA}}^0 \equiv \nu_{\text{SSA}}(t=0)$ , an increase in flux of the synchrotron emission at a given frequency  $\nu^* > \nu_{\text{SSA}}^0$  is expected at time  $t^*$  such that  $\nu_{\text{SSA}}(t^*) \equiv \nu_{\text{SSA}}^* \approx \nu^*$ , when the source is characterised by a size  $R^* = R(t^*)$  and  $B^* = B(t^*)$ . Hence, at the time  $t^*$  the values of  $R^*$  and  $B^*$  are such that the source is optically thin at frequencies  $\nu \geq \nu^*$ . We use Equation 6 to relate the two frequencies  $\nu_{\text{SSA}}^0$  and  $\nu_{\text{SSA}}^*$  to the corresponding blob radius  $R^*$ :

$$\frac{\nu_{\text{SSA}}^*}{\nu_{\text{SSA}}^0} = \left[ \left( \frac{B^*}{B_0} \right)^{\frac{p+2}{2}} \left( \frac{R_0}{R^*} \right)^2 \right]^{\frac{2}{p+4}} = \left[ \frac{R_0}{R^*} \right]^{\frac{m_B(p+2)+4}{p+4}}. \quad (7)$$

This equation provides a link between the temporal evolution of the SSA frequency and source radius, for a homogeneous blob

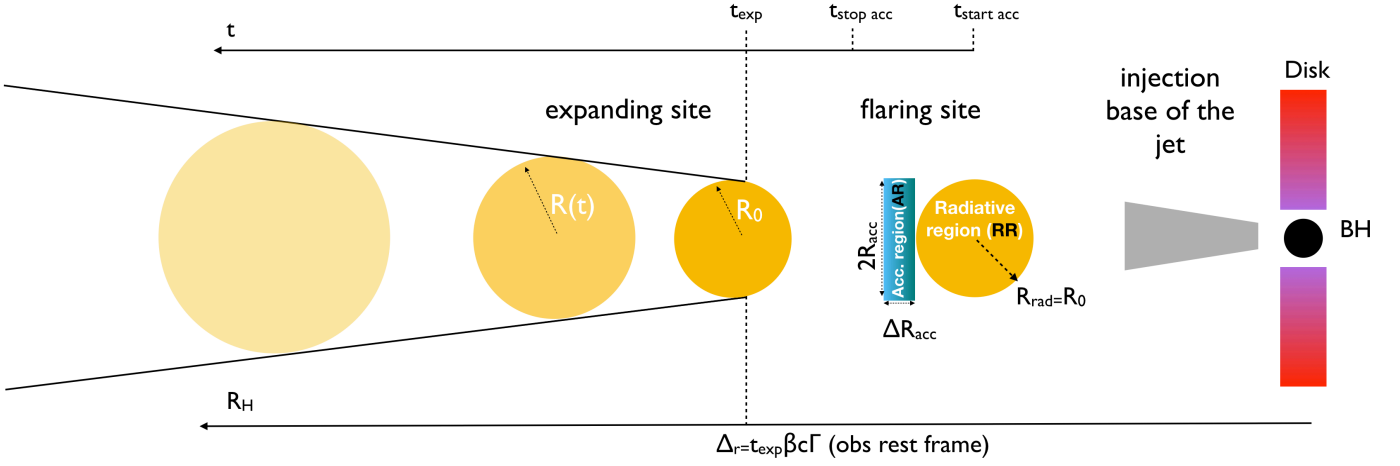


Fig. 1: Schematic representation of the model implemented in JetSeT to simulate the flaring stage and the adiabatic expansion. At time  $t_{\text{start acc}}$ , particles are injected and accelerated in the acceleration region where they undergo both cooling and acceleration processes and diffuse towards the radiative region, where only losses take place. The acceleration process ends at time  $t_{\text{stop acc}}$ . After a time  $t_{\text{exp}}$ , the expansion process takes place in the RR region.

expanding with a constant velocity. We can easily invert this relation, and solve it in terms of  $R^*$ :

$$R^* = R_0 \left( \frac{\nu_{\text{SSA}}^0}{\nu_{\text{SSA}}^*} \right)^\psi \quad (8)$$

$$\psi = \frac{p + 4}{m_B(p + 2) + 4}.$$

This equation allows us to determine the time needed, starting from  $t_{\text{exp}}$ , to move the initial  $\nu_{\text{SSA}}^0$  to  $\nu_{\text{SSA}}^*$ , which is also the time needed to expand the source from an initial radius  $R_0$  to the radius  $R^*$ . The corresponding time to reach the peak of the synchrotron light curve at the frequency  $\nu_{\text{SSA}}^*$  in the blob rest frame is

$$t_{\text{peak}} = \Delta t_{R_0 \rightarrow R^*} = \frac{R^* - R_0}{\beta_{\text{exp}} c} = \frac{R_0}{\beta_{\text{exp}} c} \left[ \left( \frac{\nu_{\text{SSA}}^0}{\nu_{\text{SSA}}^*} \right)^\psi - 1 \right]. \quad (9)$$

We stress that this equation holds as long as the synchrotron cooling is not the dominant cooling timescale, and we discuss this topic more in detail in Section 5. The total delay will be given by the sum of  $t_{\text{exp}}$  and  $t_{\text{peak}}$ , that is,

$$\Delta t_{\nu_{\text{SSA}}^0 \rightarrow \nu_{\text{SSA}}^*} = t_{\text{exp}} + t_{\text{peak}} = t_{\text{exp}} + \frac{R_0}{\beta_{\text{exp}} c} \left[ \left( \frac{\nu_{\text{SSA}}^0}{\nu_{\text{SSA}}^*} \right)^\psi - 1 \right]. \quad (10)$$

Finally, the adiabatic decay time will be proportional to the adiabatic cooling time at  $R^*$ :

$$t_{\text{decay}}^{\text{ad}}(t^*) \propto \frac{R^*}{\beta_{\text{exp}} c} = \frac{R_0}{\beta_{\text{exp}} c} \left( \frac{\nu_{\text{SSA}}^0}{\nu_{\text{SSA}}^*} \right)^\psi. \quad (11)$$

Of course, this is the relevant timescale at the time  $t^*$  such that  $R(t^*) = R^*$ , and will increase according to Equation 4. It is relevant to note that the decaying time will also be affected by the purely geometric factor, depending on  $B(t)$  and  $R(t)$ , that is, the flux variation due to a change in  $B(t)$  and  $R(t)$ , ignoring the cooling terms. This can be easily derived from the expected synchrotron trend for an optical depth  $\tau \gg 1$ ,  $F_{\nu_{\text{SSA}}}(t) \propto N(t)V(t)B(t)^{-0.5}$  (Ghisellini 2013), and taking into account that, for confined emitters,  $N(t)V(t)$  is constant:  $F_{\nu_{\text{SSA}}}(t) \propto B(t)^{-0.5}$ , where  $V(t)$  is the time-dependent value of the blob volume.

Hence, the time-dependent geometric decay time at  $t = t^*$  will read

$$t_{\text{decay}}^{\text{geom}}(t^*) \propto \frac{F_{\nu_{\text{SSA}}}(t^*)}{\dot{F}_{\nu_{\text{SSA}}}(t^*)} \propto \frac{R^*}{m_B \beta_{\text{exp}} c} = \frac{t_{\text{decay}}^{\text{ad}}(t^*)}{m_B}. \quad (12)$$

Therefore, within the assumptions described above, and as long as the adiabatic cooling timescale dominates over the synchrotron one, we can estimate the final decay timescale as

$$t_{\text{decay}}(t^*) \propto \frac{R_0}{m_B \beta_{\text{exp}} c} \left( \frac{\nu_{\text{SSA}}^0}{\nu_{\text{SSA}}^*} \right)^\psi. \quad (13)$$

The balance between the relevant timescales is quite complex, and in Figure 2 we show the trends for different configurations. The left panels refer to the case of  $\beta_{\text{exp}} = 0.1$ , and the right panels to the case of  $\beta_{\text{exp}} = 0.001$ . We select the boundaries  $\gamma = 10$  and  $\gamma = 1000$  to sample typical values of the Lorentz factor corresponding to electrons radiating by synchrotron emission in the radio band, for  $B$  ranging in  $[0.001, 1]$  G, and a broad range of values of  $\delta$  and  $z$ . We notice that for  $\beta_{\text{exp}} = 0.1$ , the adiabatic and geometrical decay timescales dominate over the synchrotron timescale, except for the initial state of a few configurations. On the contrary, for the case of  $\beta_{\text{exp}} = 0.001$  the competition between radiative and adiabatic timescales is more complex. The effect of this complex interplay among the cooling timescales is investigated in detail in Section 5. We also notice that, for the parameter space investigated in the present analysis, the crossing time is always shorter than the other timescales, making the approximation of ignoring its effect hereafter relatively plausible.

Finally, we can express these relations—which are valid in the adiabatic-dominated cooling regime—in the observer frame:

$$\Delta t_{\nu_{\text{SSA}}^0, \text{obs} \rightarrow \nu_{\text{SSA}}^*, \text{obs}} = \frac{1+z}{\delta} \left[ t_{\text{exp}} + \frac{R_0}{\beta_{\text{exp}} c} \left( \left( \frac{\nu_{\text{SSA}}^0}{\nu_{\text{SSA}}^*} \right)^\psi - 1 \right) \right] \quad (14)$$

$$t_{\text{decay}}^{\text{obs}} = \frac{(1+z)}{\delta} \frac{R_0}{m_B \beta_{\text{exp}} c} \left( \frac{\nu_{\text{SSA}}^0}{\nu_{\text{SSA}}^*} \right)^\psi$$

$$t_{\text{peak}}^{\text{obs}} = \frac{(1+z)}{\delta} \frac{R_0}{\beta_{\text{exp}} c} \left[ \left( \frac{\nu_{\text{SSA}}^0}{\nu_{\text{SSA}}^*} \right)^\psi - 1 \right],$$

where  $\nu^{\text{obs}} = \nu \frac{\delta}{z+1}$ , and the  $\delta$  is a beaming factor:

$$\delta = \frac{1}{\Gamma(1 - \beta_{\Gamma} \cos(\theta))}, \quad (15)$$

where  $\Gamma$  is the bulk Lorentz factor of the blob moving with velocity  $\beta_{\Gamma}c$ , and  $\theta$  is the observing angle of the jet. We can substitute the observed timescale variability  $t_{\text{var}}^{\text{obs}} = \frac{(1+z)R_0}{\delta c}$  in the equations above:

$$\begin{aligned} \Delta t_{\nu_{\text{SSA}}^{\text{obs}} \rightarrow \nu_{\text{SSA}}^{\ast, \text{obs}}} &= t_{\text{exp}}^{\text{obs}} + \frac{t_{\text{var}}^{\text{obs}}}{\beta_{\text{exp}}} \left[ \left( \frac{\nu_{\text{SSA}}^0}{\nu_{\text{SSA}}^{\ast, \text{obs}}} \right)^{\psi} - 1 \right] \\ t_{\text{peak}}^{\text{obs}} &= \frac{t_{\text{var}}^{\text{obs}}}{\beta_{\text{exp}}} \left[ \left( \frac{\nu_{\text{SSA}}^0}{\nu_{\text{SSA}}^{\ast, \text{obs}}} \right)^{\psi} - 1 \right] \\ t_{\text{decay}}^{\text{obs}} &= \frac{t_{\text{var}}^{\text{obs}}}{m_B \beta_{\text{exp}}} \left( \frac{\nu_{\text{SSA}}^0}{\nu_{\text{SSA}}^{\ast, \text{obs}}} \right)^{\psi}, \end{aligned} \quad (16)$$

where  $t_{\text{exp}}^{\text{obs}} = t_{\text{exp}}(1+z)/\delta$ . The distance travelled along the jet during the time interval  $\Delta t_{\nu_{\text{SSA}}^{\text{obs}} \rightarrow \nu_{\text{SSA}}^{\ast, \text{obs}}}$  will be

$$\Delta r = \Gamma \Delta t_{\nu_{\text{SSA}}^{\text{obs}} \rightarrow \nu_{\text{SSA}}^{\ast, \text{obs}}} \beta_{\Gamma} c = \frac{\delta \Gamma \beta_{\Gamma} c \Delta t_{\nu_{\text{SSA}}^{\text{obs}} \rightarrow \nu_{\text{SSA}}^{\ast, \text{obs}}}}{1+z}, \quad (17)$$

which is in agreement with the phenomenological derivations by Pushkarev et al. (2010) and Max-Moerbeck et al. (2014), if  $\nu_{\text{SSA}}^{\text{obs}}$  corresponds to the initial observed SSA frequency at the time of the flaring episode, and  $\nu_{\text{SSA}}^{\ast, \text{obs}}$  corresponds to the observed frequency of the delayed radio flare.

### 3. Self-consistent temporal evolution of an expanding blob with the JetSeT code.

To follow the evolution of the emitting particle distribution, and the radiative fields, we use the `JetTimeEvol` class from the `jet_timedep` module of the open-source `JetSeT`<sup>1</sup> framework (Tramacere 2020; Tramacere et al. 2011; Tramacere et al. 2009). This class allows the user to evolve the particle distribution under the effects of radiative cooling, adiabatic expansion, and acceleration processes (both systematic and stochastic), and to extract SEDs and light curves at any given time (see Appendix A for further details on code availability and reproducibility). The code proceeds through the numerical solution of a kinetic equation, following the same approach as in Tramacere et al. (2011) based on the employment of the quasi-linear approximation with the inclusion of a momentum diffusion term (Ramaty 1979; Becker et al. 2006). The equation governing the temporal evolution of the particle energy distribution  $n(\gamma) = dN(\gamma)/d\gamma$  is the Fokker-Planck (FP) equation that reads

$$\begin{aligned} \frac{\partial n(\gamma, t)}{\partial t} &= \frac{\partial}{\partial \gamma} \left\{ - [S(\gamma, t) + D_A(\gamma, t)] n(\gamma, t) \right\} \\ &+ \frac{\partial}{\partial \gamma} \left\{ D_p(\gamma, t) \frac{\partial n(\gamma, t)}{\partial \gamma} \right\} - \frac{n(\gamma, t)}{T_{\text{esc}}(\gamma)} - \frac{n(\gamma, t)}{T_{\text{ad}}(t)} + Q(\gamma, t). \end{aligned} \quad (18)$$

The momentum diffusion coefficient  $D_p(\gamma, t) \propto (\gamma^q)$  (Becker et al. 2006) and the average energy change term resulting from the momentum-diffusion process  $D_A(\gamma, t) = (2/\gamma)D_p(\gamma, t)$  (Becker et al. 2006) represent the contribution from a stochastic momentum-diffusion acceleration mechanism (Kardashev 1962;

Melrose 1969; Katarzyński et al. 2006; Stawarz & Petrosian 2008). The systematic term  $S(\gamma, t) = -C(\gamma, t) + A(\gamma, t)$  describes systematic energy loss ( $C$ ) and/or gain ( $A$ ), and  $Q(\gamma, t)$  is the injection term. A detailed description of the cooling terms and the diffusion coefficient is provided in Appendix B. The term  $\frac{n(\gamma, t)}{T_{\text{ad}}}$  corresponds to the decrease in particle density due to the expansion process, with  $T_{\text{ad}}(t) = \frac{1}{3} \frac{R(t)}{\beta_{\text{exp}} c}$  (Gould 1975). This term is connected to source geometry and should not be confused with the cooling term defined in Equation 4 and plugged in the  $C(\gamma, t)$  term (see Appendix B). The term  $\frac{n(\gamma, t)}{T_{\text{esc}}(\gamma)}$  represents the particle escape term. The injection function  $Q(\gamma_{\text{inj}}, t)$  is normalised according to

$$L_{\text{inj}} = V_{\text{acc}} \int \gamma m_e c^2 Q(\gamma, t) d\gamma \quad (\text{erg/s}), \quad (19)$$

where  $V_{\text{acc}}$  is the volume of the acceleration region, and the integration is performed over the numerical grid used to solve Equation 18 (see the following section for further details). The numerical solution of the FP equation is obtained using the same approach as Tramacere et al. (2011), which is based on the method proposed by Chang & Cooper (1970) as described in Park & Petrosian (1996).

Table 1: Parameters for the flaring simulation

		rad. region	acc. region
$R$	(cm)	$5 \times 10^{15}$	$5 \times 10^{15}$
$\Delta R^{\text{acc}}$	(cm)	-	$5 \times 10^{14}$
$R_{H0}$	(cm)	-	$10^{17}$
$B$	(G)	0.2	0.2
$\delta$		30	30
$z$		0.03	0.03
$L_{\text{inj}}$	(erg/s)	$5 \times 10^{39}$	-
$q$		-	2
$t_A$	(s)	-	$2.5 \times 10^4$
$t_{D_0} = 1/D_{P0}$	(s)	-	$1.5 \times 10^5$
$T_{\text{esc}}$	(s)	$\infty$	$5 \times 10^4$
<i>Duration</i>	(s)	$10^6$	$10^6$
<i>Duration acc.</i>	(s)	-	$10^5$
<i>Duration inj.</i>	(s)	-	$10^5$
$T_{\text{size}}$		$2 \times 10^4$	$2 \times 10^4$
$NUM_{\text{SET}}$		200	200
$\gamma_{\text{inj}}$		-	10.0

Table 2: Parameters for the long-term simulation with expansion

		expanding rad. region
$R_0$	(cm)	$5 \times 10^{15}$
$B_0$	(G)	0.2
$\delta$		30
$m_B$		1
$\beta_{\text{exp}}$	(c)	[0.001 – 0.3]
$t_{\text{exp}}$	(s)	$1 \times 10^7$
$T_{\text{esc}}$	(s)	$\infty$
<i>Duration</i>	(s)	$[1.6 \times 10^7 - 1.9 \times 10^9]$
$T_{\text{size}}$		$[1.6 \times 10^4 - 1.8 \times 10^6]$
$NUM_{\text{SET}}$		[1000, 5000]

<sup>1</sup> <https://github.com/andreatramacere/jetset>

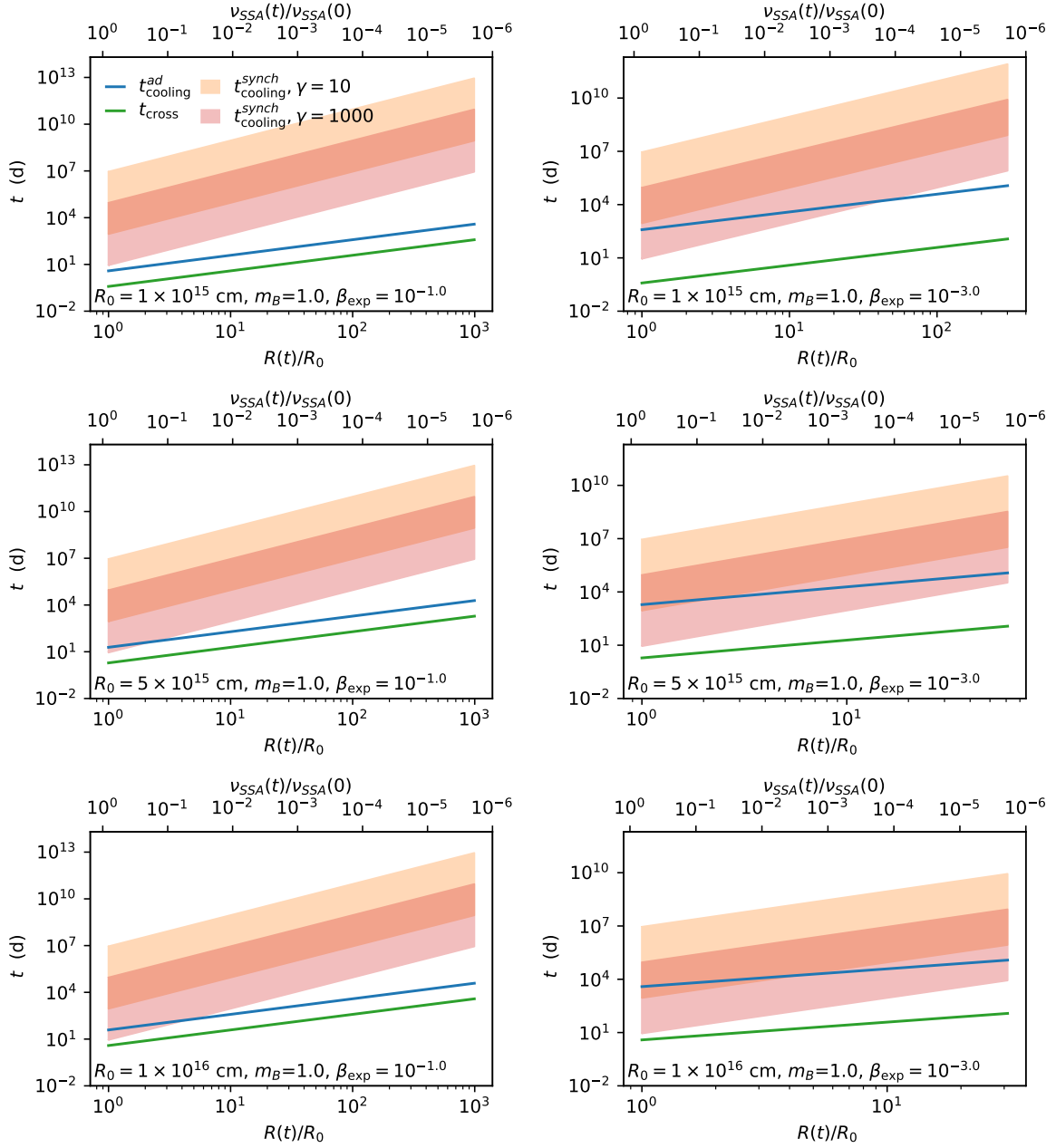


Fig. 2: Competition among the different timescales. *Left panels*: Case of  $\beta_{\text{exp}} = 0.1$ . *Right panels*: Case of  $\beta_{\text{exp}} = 0.001$ . The top row refers to the case of  $R_0 = 1 \times 10^{15}$  cm, the middle row to the case of  $R_0 = 5 \times 10^{15}$  cm, and the bottom row to the case of  $R_0 = 1 \times 10^{16}$  cm. The times are in the blob frame, and the total duration is such that  $R(t_{\text{stop}}) = 1000R_0$ . The  $x$  axis reports on the bottom side the value of  $R(t)/R_0$ , whilst on the opposite side the corresponding value of  $v_{\text{SSA}}(t)/v_{\text{SSA}}(0)$  is reported, for the case of no particle escape. The orange shaded area represents the synchrotron cooling timescales, with the lower bound corresponding to the case of  $\gamma = 10$  and  $B_0 = 1.0$  G, and the upper bound corresponding to the case of  $\gamma = 10$  and  $B_0 = 0.01$  G. The red shaded area, represents the same trend for the case of  $\gamma = 1000$ . The blue line represents the adiabatic cooling time (Equation 4), the black red line represents the geometrical decay time (Equation 12), and the green line the light crossing time  $(R(t)/c)$ .

### 3.1. General setup of the simulation, assumptions, and limitations

We set up our simulation in order to reproduce an initial flaring episode, and a following expansion process within a leptonic synchrotron self-Compton (SSC) scenario. During the flare, particles are injected and accelerated in the acceleration region (AR) where they undergo both cooling and acceleration processes, and diffuse toward the radiative region (RR), where only losses take place. After a time  $t_{\text{exp}}$  (measured in the blob frame), the expansion

process takes place in the RR region. We follow the long-term evolution under the effects of radiative cooling and adiabatic expansion, setting the duration of the simulation to be long enough to follow the particle evolution due to the expansion process. A schematic representation of these processes is shown in Figure 1.

In the current approach, the values of the magnetic field ( $B$ ) and the radius ( $R$ ) in the RR during the flaring episode are taken from the typical values derived from MW modelling for HBLs, and these values coincide with the initial values at the begin-

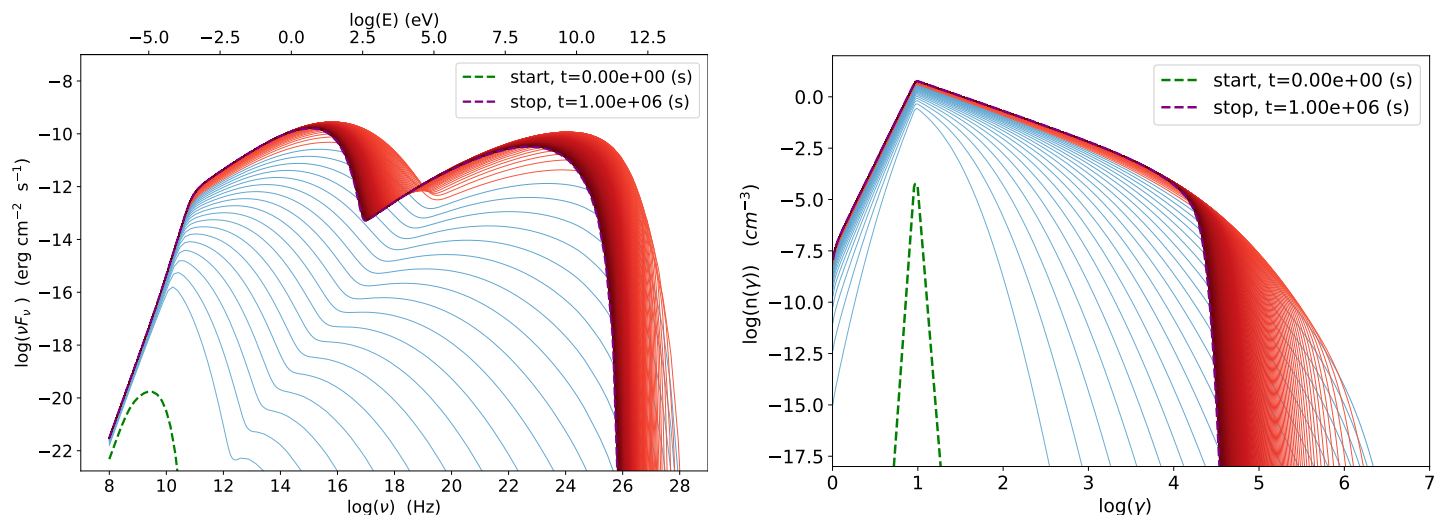


Fig. 3: *Left panel*: SEDs corresponding to the simulation of the flaring state, for the radiative region. The dashed green line corresponds to the earliest of the SEDs stored by the code, the blue lines correspond to the period when the injection, acceleration, and radiative process are active, and the red lines correspond to the period when only the radiative processes are active. The times reported in the label are in the blob frame. *Right panel*: Same as in left panel, but for the electron energy distribution in the radiative region.

ning of the expansion ( $B_0$  and  $R_0$ ). Hence, we only extrapolate the evolution of  $B$  according to  $m_B$  and  $R(t)$  from the beginning of the expansion process. We adopt this approximation for the current approach because we are mostly interested in the determination of the radio- $\gamma$  response in terms of delay and expansion velocity, and are not interested in investigating the jet structure before the flaring site. Nevertheless, our model can be easily generalised to a generic conical jet geometry simply by replacing the temporal law  $R(t)$  in order to follow the jet cross-section as a function of the jet opening angle and of the distance from the BH, setting a scaling parameter  $z(t) = R_H(t)/R_{H0}$ , and then expressing  $R(t) = R_0 z(t)^{m_R}$ , and  $B(t) = B_0 z(t)^{-m_B m_R}$ , where the expansion index of the jet  $m_R$  is assumed to be  $\in [0, 1]$ . In the ballistic case ( $m_R = 1$ , Kaiser 2006) the initial opening angle of the jet will be given by  $\tan \theta_0 = R_0/R_{H0}$ , and will change with  $z$  according to  $\tan(\theta(z)) = \tan(\theta_0)(R_H(t)/R_{H0})^{m_R-1}$ , i.e. will be constant.

Both for the flaring and long-term (expansion) simulations, the time grid for the solution of the FP equation is tuned to have a temporal mesh at least two orders of magnitude smaller than the shortest cooling and acceleration timescale. We use an energy grid with 1500 points and  $1 \leq \gamma \leq 10^8$ . As the total number of time steps used in the FP numerical solution ( $T_{size}$ ) can be very large, a subsample of the time steps of the simulation ( $NUM_{SET}$ ) is stored in arrays, and can be used to build both light curves and SEDs. In the current simulation, we use  $NUM_{SET} = 200$  for the flaring stage and  $NUM_{SET} \in [1000, 5000]$  for the long-term evolution, depending on the duration of the simulation. This guarantees an adequate time sampling for light curves and spectral evolution. SEDs are computed from the stored electron distributions, and from the blob parameters (according to their temporal evolution). In our case, the blob variable parameters are the source radius ( $R$ ) and magnetic field ( $B$ ), which evolve according to Equations 1 and 2, respectively. Light curves are obtained by integrating SEDs between two frequencies, or as monochromatic. The code offers the possibility to convolve the light curves with the light-crossing time. In the present analysis, we skip this option because, as shown in section 2, the light-crossing time is always shorter than the other competing timescales. This ap-

proximation used in the current approach will be removed in a forthcoming paper, where it will be treated accurately. We also decided to use a constant bulk Lorentz factor. We tested and verified that, for the current scope of the simulations, the difference between enabling and disabling the IC cooling is negligible, and therefore to speed up the computational time we use only synchrotron cooling for the radiative terms.

### 3.2. Flare simulation

To generate the flaring event, we use the `JetTimeEvol` configuration with a separated acceleration and radiative region. With this configuration, particles are injected into the acceleration region (AR), and then diffused toward the radiative region (RR) for a timescale corresponding to the flare duration. We set the parameters for the flaring stage in order to reproduce the typical SED of HBLs, according to Tramacere et al. (2011). We assume that both radiative and first and second-order acceleration processes, occur in the AR, whilst in the RR region, we only take cooling processes into account. Particles are injected in the AR with a quasi-monoenergetic distribution, normalised according to Equation 19. This initial distribution evolves under the effect of radiative and accelerative mechanisms, leading to the formation of a distribution with a low-energy power-law branch that bends close to the equilibrium energy. The high-energy branch exhibits a log-parabolic shape during the acceleration-dominated stage, and approaches a relativistic Maxwellian cut-off at the equilibrium. The spectral index of the low-energy power law is dictated by the ratio of the first-order acceleration timescale to the escape time from the acceleration region, whilst the curvature during the acceleration-dominated stage is dictated by the momentum diffusion term. The acceleration region is modelled as a cylindrical shell with a radius equal to the radiative region, and we assume a ten times smaller width. Particles leaving the acceleration region (shock front) enter the radiative region with a rate derived from the escape probability  $P_{escape}(\Delta t_{mesh}) = 1 - \exp(-\Delta t_{mesh}/T_{esc})$  (Park & Petrosian 1996), where  $\Delta t_{mesh}$  is the temporal mesh for the numerical solution of the FP

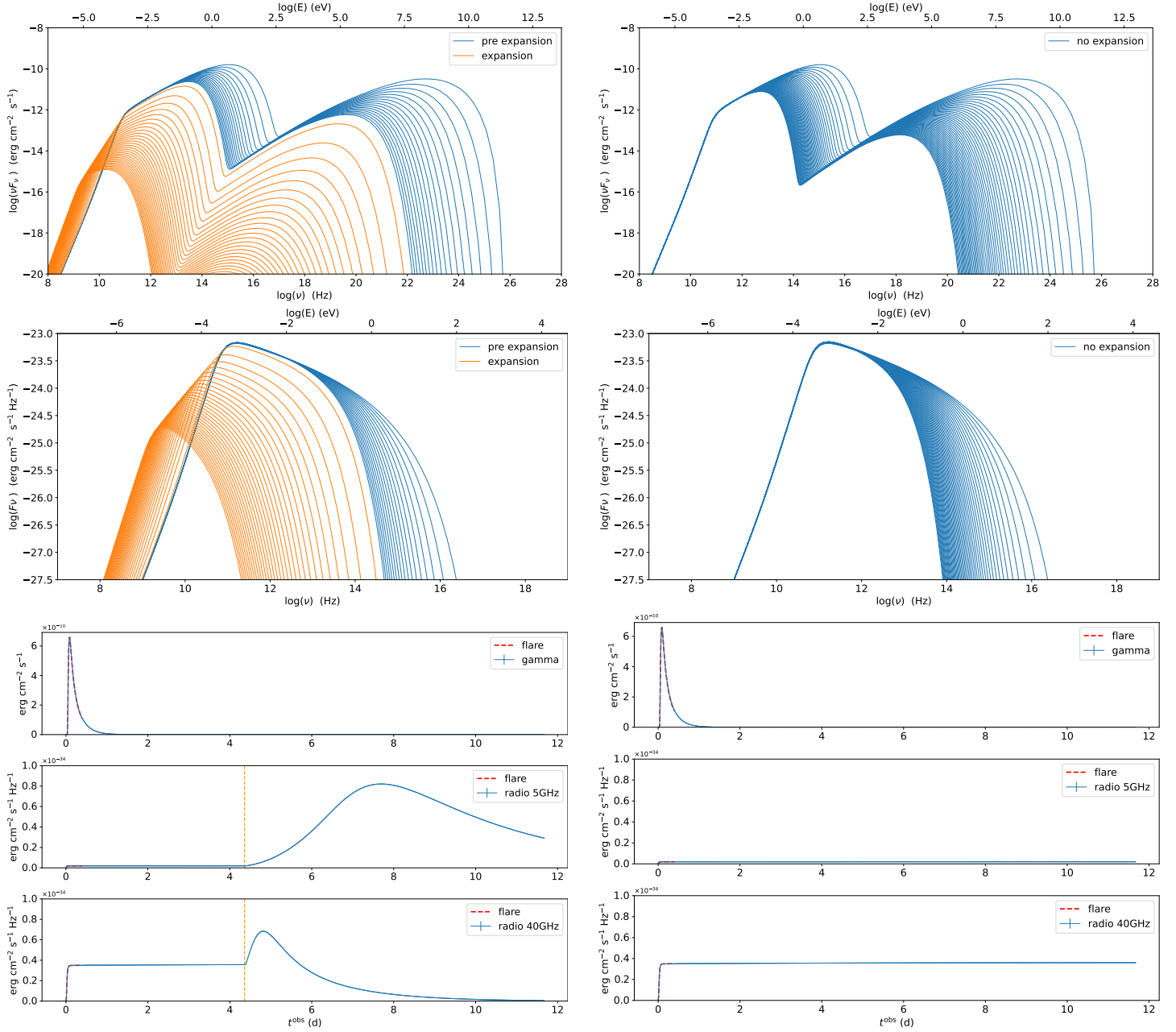


Fig. 4: Comparison of non-expanding (*right panels*) vs expanding (*left panels*) for  $\beta_{\text{exp}} = 0.1$ . The *top panels* show the evolution of the SEDs after the flaring stage, where the blue colour indicates the non/pre-expansion case, and orange indicates the expansion. The second row of panels shows the evolution of the flux density ( $F_\nu$ ). The three *bottom panels* show the merged light curves of both the flaring and the long-term simulation in the Fermi-LAT band, and at 5 and 40 GHz. The red dashed lines mark the light-curve segment belonging to the flaring stage and the orange vertical dashed lines mark the beginning of the expansion.

equation. The radiative region is modelled with a spherical geometry, where only the cooling processes are active and where we assume that particles are confined ( $T_{\text{esc}} \gg \text{Duration}$ ). The position along the jet of the flaring region is placed at  $R_{H0} = 10^{17}$  cm. Particles are injected and accelerated in the AR for a duration equal to  $\text{Duration acc.}$  and equal to  $\text{Duration inj.}$ , respectively. The total time-span of the flare simulation is given by the parameter  $\text{Duration}$ . The parameters for the acceleration and radiative region are reported in Table 1.

### 3.3. Long-term simulation of the expanding radiative region

The long-term simulation is an extension of the flaring event over a longer timescale, only for the RR, and without injection or particle escape. The duration of the simulation for the long-term evolution is estimated according to  $T_{\text{long}} = \Delta t_{v_{\text{SSA}}(0) \rightarrow v_{\text{SSA}}(t)} + 10 t_{\text{decay}}$ . We set the expansion time  $t_{\text{exp}} = 10^7$  s, and we evaluate ten realizations of the process, with  $\beta_{\text{exp}}$  evaluated on a ten-point logarithmic grid [0.001, 0.3] to evaluate the trends as a function of  $\beta_{\text{exp}}$ . We realise a further simulation with  $\beta_{\text{exp}} = 0.1$  to investigate the trends as a function of the radio frequency. The parameters for the acceleration and radiative region are reported in Table 2. We stress that the initial position of the flaring region

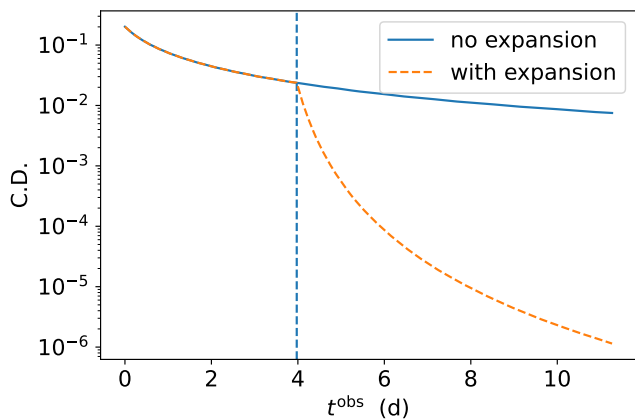


Fig. 5: The CD versus the time of the simulation in the observer frame. The CD is evaluated as the ratio of the peak flux of the IC component to the peak flux of the S component. The vertical dashed line marks the beginning of the expansion (for the expanding case, orange line). It is clear that when the adiabatic expansion begins, the IC starts to drop rapidly as a consequence of the larger volume and lower seed photons density.

$R_{H0}$  can be changed without loss of generality, because there is no dependence of any relevant timescale on  $R_{H0}$  in our model.

#### 4. Comparison of non-expansion versus expansion

In this section, we compare the different behaviours of the spectral evolution when the adiabatic expansion is active or switched off. For this purpose, we use the value of  $\beta_{\text{exp}} = 0.1$ . The results are shown in Figure 4, where the plots in the left column refer to the expansion case and the plots in the right column refer to the non-expansion case. The top panels show the evolution of the SEDs, after the flaring stage, where the blue flags mark the non-expanding and pre-expansion cases, and the orange flags mark the case with expansion. We note that, in the non-expanding simulation, the evolution follows the usual pattern dictated by the radiative cooling timescales. On the contrary, in the expanding case, we notice that when the expansion starts, the patterns in both the synchrotron and IC components are different. The IC component is mainly affected by a significant drop in the Compton dominance (CD). This can be better appreciated in Figure 5, where we plot the CD versus the time of the simulation. The CD is evaluated as the ratio of the peak flux of the IC component to the peak flux of the S component. The vertical dashed line marks the beginning of the expansion (for the expanding case, orange line). It is clear that when the adiabatic expansion begins, the IC starts to drop rapidly, as a consequence of the larger volume and lower seed-photon density. This is a very interesting feature, and might already be visible during the flaring stage. The most integrating effect, for our analysis, is the evolution of the S component. On top of the flux decay dictated by the adiabatic losses, and decreased magnetic field, we notice the shift in the SSA frequency, which is absent in the non-expanding case. This effect can be better appreciated in the second row of panels in Figure 4, where we plot the evolution of the flux density ( $F_\nu$ ). Whilst in the non-expanding case the SSA is almost stable at the initial value of  $\approx 10^{11}$  Hz, in the expanding case the SSA decreases with time as predicted by Equation 5. The actual trend will be investigated in detail in the following two sections. The three bottom panels of Figure 4 show the light curves in the Fermi-LAT band, and at 5 and 40 GHz. We notice that, in the

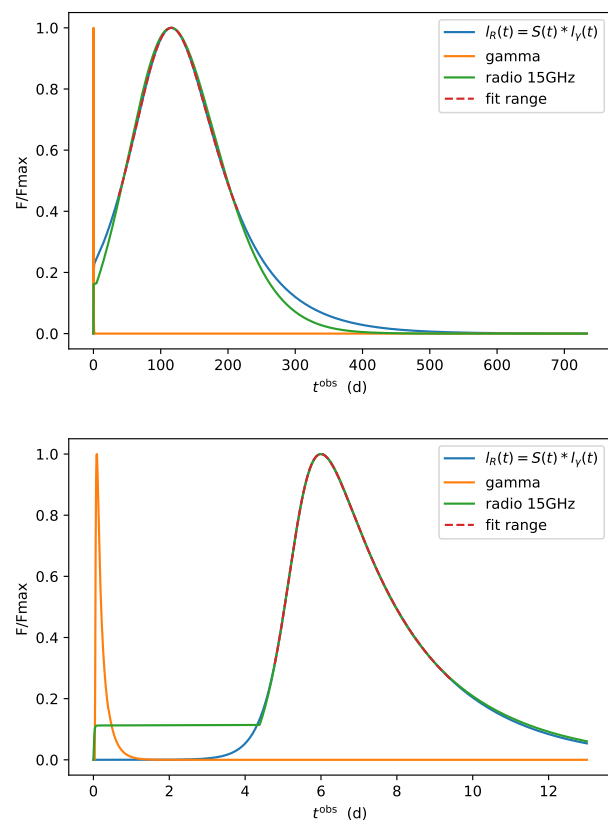


Fig. 6: Best fit for the radio- $\gamma$  response at 15 GHz for  $\beta_{\text{exp}} = 0.001$  (top panel) and at 15 GHz for  $\beta_{\text{exp}} = 0.084$  (bottom panel), and  $t_{\text{exp}} = 1 \times 10^7$  s. All other parameters are the same as reported in Table 2. The light curves are in the observer frame. The red dashed line represents the actual fit interval, the orange line represents the simulated  $\gamma$ -ray light curve, the green line the simulated radio light curve, and the blue line is the best fit of the radio light curve obtained from the convolution of the  $\gamma$ -ray light curve with the best-fit response. The  $\gamma$ -ray light curve is the same in both panels, and appears different due to the different duration of the simulations.

non-expanding case, the temporal behaviour is again in agreement with a purely radiative cooling without particle escape. On the contrary, in the expanding case, we notice that for the radio light curves an increase in the flux level happens after the beginning of the expansion, with the time of the maximum happening earlier at larger frequencies. This can be quantitatively understood by looking at the flux density panel, which shows that the SSA moves from the initial (non-expanding case) down to lower frequencies. We quantify these delays and the different rise and decay times in the following two sections.

#### 5. Radio- $\gamma$ response and physical trends in the delay

In this section, we verify that the phenomenological trends derived in Section 2 are reproduced in our simulations and whether or not they can be applied to observed data. The empirical determination of delays is usually done by means of a discrete correlation function (DCF). A further and more interesting step is to determine a response function  $S(t)$  such that radio light curves ( $I_R$ ) can be reproduced as a ‘response’ of the  $\gamma$ -ray light curves

( $l_\gamma$ ) as a convolution (Türler et al. 1999; Sliusar et al. 2019a,b) according to

$$l_R(t) = S(t) * l_\gamma(t), \quad (20)$$

where the  $S$  is an empirical function that depends on parameters that can be related to the observable quantities investigated in Section 2. We propose the following response function:

$$S(t) = A \frac{\exp\left(-\frac{t-\Delta}{t_f}\right)}{1 + \exp\left(-\frac{t-\Delta}{t_f}\right)}, \quad (21)$$

where  $t_f$  is the decay time, and  $t_r$  is the rise time.

This is the combination of a logistic function for the rising part and an exponential decay for the decaying part, with  $A$  being a scaling factor. The scaling factor depends mainly on the initial value of the Compton dominance, on the observed radio frequency, and on  $m_B$ . In the present analysis, we are not investigating its impact. The peak of  $S(t)$ , corresponding to the radio- $\gamma$  delay, reads

$$\Delta t = \Delta - t_u \ln\left(\frac{t_u}{t_f - t_u}\right). \quad (22)$$

The actual determination of the rise and decay time is analytically complicated. We estimated  $t_{\text{rise}}$  and  $t_{\text{decay}}$  numerically by imposing the condition  $S(t) = \frac{A}{2}$  for  $t_{\text{rise}}$  and  $S(t) = \frac{A}{e}$  for  $t_{\text{decay}}$ , and verified that within a maximum deviation of 5% for  $t_{\text{rise}}$ , and of 0.2% for  $t_{\text{decay}}$ , these timescales can be evaluated according to

$$t_{\text{rise}} = t_u \left(0.54 + 1.34 \left(\frac{t_f}{t_u}\right)^{1/4}\right) \quad (23)$$

$$t_{\text{decay}} = t_f \left(1.00 + 1.33 \left(\frac{t_f}{t_u}\right)^{-1.11}\right). \quad (24)$$

For the propagation of the uncertainties we used the `Uncertainties`<sup>2</sup> Python package.

### 5.1. Validation of phenomenological relations

Before investigating the phenomenological trends, we validate the relations in Section 2 using long-term simulations with ten different values of  $\beta_{\text{exp}}$  evaluated on a logarithmic grid ranging [0.001, 0.3]. We use two scenarios: one where we disable only the radiative cooling term in the FP equation, and one with both radiative and adiabatic cooling terms enabled. As the phenomenological relations derived in Section 2 are valid when the adiabatic cooling is dominant, the deviations in the trends with the radiative cooling enabled will highlight the effect of the competition between the synchrotron cooling and time the adiabatic time already discussed in Section 2. In order to estimate the trends, we minimise the right-hand side of Equation 20 with respect to the left-hand side, where  $l_\gamma$  and  $l_R$  are the light curves produced in the simulations, leaving as free parameters  $A$ ,  $\Delta$ ,  $t_u$ , and  $t_f$ . To perform the analysis in the observer frame, we express Equations 14 in terms of  $R_{\text{obs}}^0 = R_0 \frac{1+z}{\delta}$  and of the observed radio frequencies:

$$t_{\text{decay}}^{\text{obs}} = \frac{R_0^{\text{obs}}}{m_B \beta_{\text{exp}} c} \left(\frac{\nu_{\text{SSA}}^{0,\text{obs}}}{\nu_{\text{SSA}}^{*,\text{obs}}}\right)^\phi \quad (25)$$

$$t_{\text{rise}}^{\text{obs}} = \frac{1}{2} t_{\text{peak}}^{\text{obs}} = \begin{cases} \frac{1}{2} \frac{R_0^{\text{obs}}}{\beta_{\text{exp}} c} \left[\left(\frac{\nu_{\text{SSA}}^{0,\text{obs}}}{\nu_{\text{SSA}}^{*,\text{obs}}}\right)^\phi - 1\right] & \text{if } \nu_{\text{SSA}}^{0,\text{obs}} > \nu_{\text{SSA}}^{*,\text{obs}} \\ 0 & \text{otherwise} \end{cases}$$

$$\Delta t^{\text{obs}} = t_{\text{exp}}^{\text{obs}} + t_{\text{peak}}^{\text{obs}} = t_{\text{exp}}^{\text{obs}} + \frac{R_0^{\text{obs}}}{\beta_{\text{exp}} c} \left[\left(\frac{\nu_{\text{SSA}}^{0,\text{obs}}}{\nu_{\text{SSA}}^{*,\text{obs}}}\right)^\phi - 1\right].$$

As we show later, as the value of the electron index  $p$  evolves with time, the use of  $\psi$  as a function of a constant  $p$  during the fit is inappropriate. Hence, we use a generic index  $\phi$  that is not related directly to  $p$  during the fit but still preserves the behaviour of the trends. In any case, we can still estimate the value of  $p$  from the best-fit parameters using the second Equation 8.

An example of best-fit convolution is reported in Figure 6, where we show the results of the best fit for the response at 15 GHz for the case with the cooling terms active, for  $\beta_{\text{exp}} = 0.084$  (top panel) and  $\beta_{\text{exp}} = 0.001$  (bottom panel), and  $t_{\text{exp}} = 1 \times 10^7$  s; all the other parameters are the same as reported in Table 2. The light curves are in the observer frame.

The results of the validation of Equations 25 are summarised in Figure 7, where we show the ratio of the timescales predicted by Equations 25 to the actual results obtained by the best fit of the radio- $\gamma$  response applied to the numerical simulations. The blue lines correspond to the case of only adiabatic cooling, and the orange lines to the case of only adiabatic plus radiative cooling. The green shaded area corresponds to the  $\pm 10\%$  region with respect to the prediction from Equation 25. For the decay time, we note that in the case of only adiabatic cooling, the trends in Equation 25 are valid within a maximum derivation of time  $\lesssim 1\%$  for the delay time. This is consistent with our expectations, because Equation 25 takes into account only the contribution from adiabatic cooling and from flux variations related to the geometrical expansion. When the radiative cooling is also enabled, the deviations are larger (by up to a factor of 2), with a trend that decreases for larger values of  $\beta_{\text{exp}}$ . This trend in the deviations is due to the different interplay between radiative and adiabatic cooling timescales for different expansion velocities, which we investigate in more detail below. For the rise time we observe a deviation by up to  $\approx 40\%$  for the cases of only adiabatic cooling and radiative plus adiabatic cooling. For the delay time, the deviations are  $\approx 20\%$  to  $\approx 30\%$  for the case of only adiabatic cooling, and  $\approx 20\%$  to  $\approx 160\%$  for the case of radiative plus adiabatic cooling. The variations in the decay are larger than those observed in the rise time, because the peak of the response is affected both by decay and rise times (see Equation 22). The validation shows that the phenomenological trends predict the timescales of the response when the adiabatic cooling is dominant with good accuracy, and, as anticipated in Section 5.2, can be biased by the competition between the radiative cooling time and adiabatic cooling time. A different balance between adiabatic and radiative cooling will cause not only deviation in the adiabatic-dominated trends but also significant changes in the electron energy distribution at the radio peak time for different values of  $\beta_{\text{exp}}$ . For the purpose of illustration, we show in Figure 8 the different states of the electron distributions at the time corresponding to the peak of the  $\nu_{\text{obs}} = 15$  GHz light curves, for the values of  $\beta_{\text{exp}}$  ranging [0.001, 0.3] used in our simulations. We note that, for smaller values of  $\beta_{\text{exp}}$ , the expansion process lasts longer, and the slower temporal decrease of

<sup>2</sup> `Uncertainties`: a Python package for calculations with uncertainties, Eric O. LEBIGOT, <http://pythonhosted.org/uncertainties/>

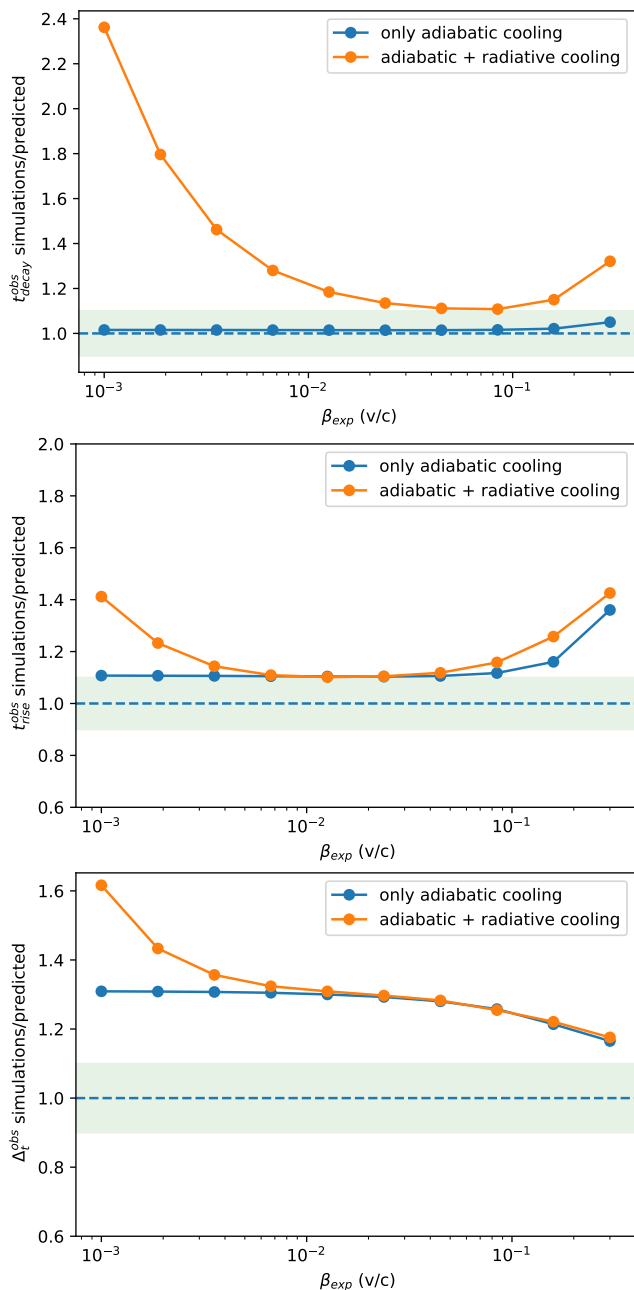


Fig. 7: Ratio of the timescales predicted by Equation 25 to the results obtained by the best fit of the radio- $\gamma$  response applied to the numerical simulations. All the other parameters are the same as reported in Table 2. The blue lines correspond to the case of only adiabatic cooling, and the orange lines to the case of radiative plus adiabatic cooling. The green shaded areas represent the  $\pm 10\%$  region with respect to the prediction from Equation 25, and the dashed horizontal lines indicate unity. *Top panel*: Radio- $\gamma$  delay. *Middle panel*: Decay time. *Bottom panel*: Rise time.

the magnetic field produces a steeper distribution with a lower cut-off of the electron distributions. On the contrary, for larger values of  $\beta_{\text{exp}}$ , the shorter duration and the faster decrease in  $B$  results in a higher cut-off of the electron distribution. In Figure 8, the dashed vertical lines represent the values of the electron Lorentz factor most contributing to the emission at  $\nu_{\text{obs}} = 15$  GHz,  $\gamma_t \approx [3\nu_{\text{SSA}}/(4\nu_L)]^{1/2}$  (Ghisellini 2013), for the different

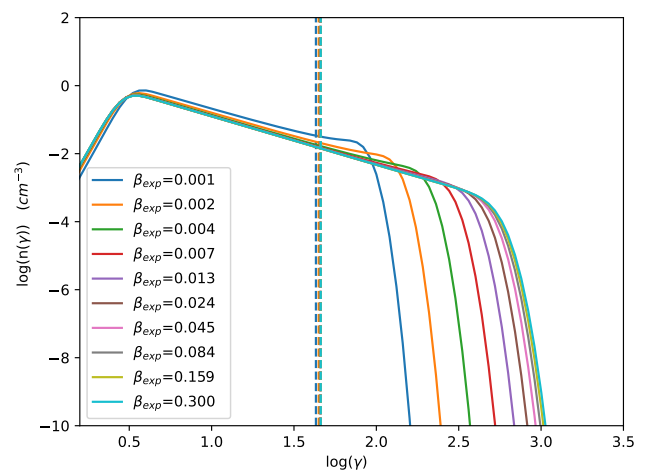


Fig. 8: State of the electron distributions at the time corresponding to the peak of the  $\nu_{\text{obs}} = 15$  GHz light curves for the expansion simulations with both radiative and adiabatic cooling enabled, and  $\beta_{\text{exp}}$  ranging [0.001, 0.3]. The vertical dashed lines correspond to the Lorentz factor of the electrons most contributing to the observed 15 GHz frequency. All the other parameters are the same as reported in Table 2

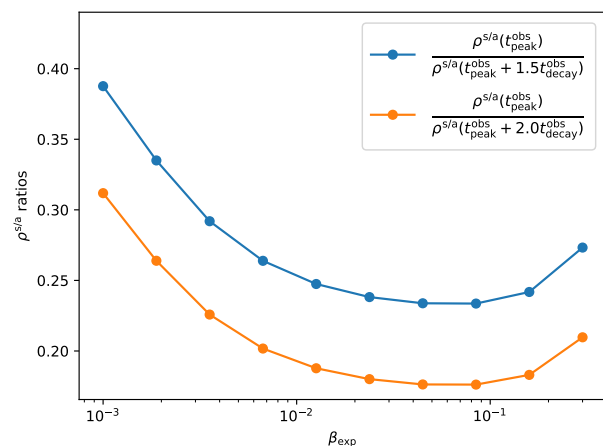


Fig. 9: Ratio of the synchrotron to adiabatic cooling timescales  $\rho^{s/a}(t) = t_{\text{sync}}(t)/t_{\text{ad}}(t)$  for the Lorentz factor of the electrons most contributing to the observed 15 GHz frequency, evaluated at  $t = t_{\text{peak}}^{\text{obs}}$  and  $t = t_{\text{peak}}^{\text{obs}} + 1.5t_{\text{decay}}^{\text{obs}}$  (blue line), and evaluated at  $t = t_{\text{peak}}^{\text{obs}}$  and  $t = t_{\text{peak}}^{\text{obs}} + 2.0t_{\text{decay}}^{\text{obs}}$  (orange line). The same values of  $\beta_{\text{exp}}$  are used as reported in Figure 8.

values of  $\beta_{\text{exp}}$ . Clearly, the corresponding value of  $p$  is different for different states of the evolution, meaning that the use of  $\psi$  as a function of a constant  $p$  is inappropriate. For these reasons we use a generic index  $\phi$  that is not related directly to  $p$ , but still preserves the behaviour of the trends.

A further effect due to the complex interplay between the cooling timescales is shown in Figure 9, where we plot the ratio of the synchrotron to adiabatic cooling timescales  $\rho^{s/a}(t) = t_{\text{sync}}(t)/t_{\text{ad}}(t)$ , for the Lorentz factor of the electrons most contributing to the observed 15 GHz frequency, evaluated at  $t = t_{\text{peak}}^{\text{obs}}$  and  $t = t_{\text{peak}}^{\text{obs}} + 1.5t_{\text{decay}}^{\text{obs}}$  (blue line), and evaluated at  $t = t_{\text{peak}}^{\text{obs}}$  and  $t = t_{\text{peak}}^{\text{obs}} + 2.0t_{\text{decay}}^{\text{obs}}$  (orange line). This complex interplay between

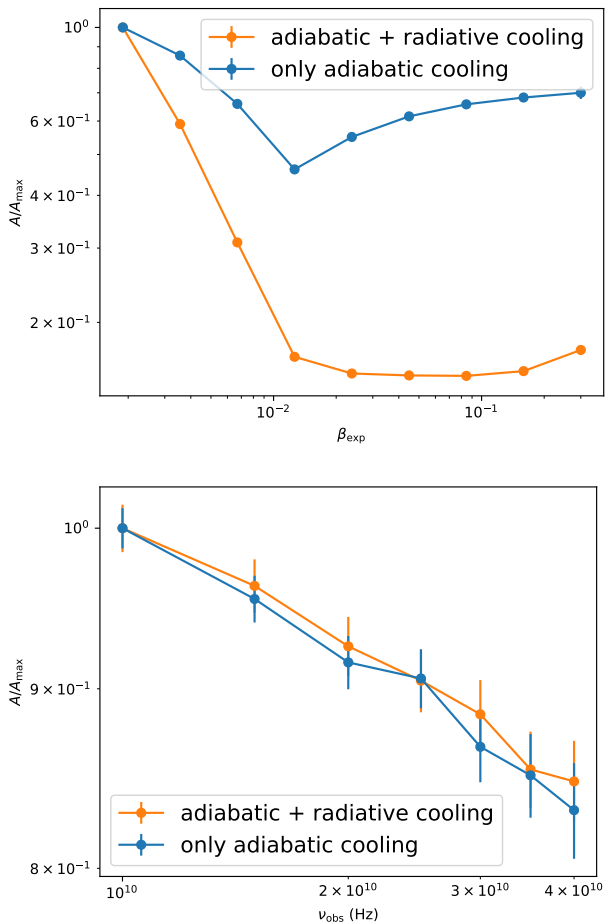


Fig. 10: *Top panel:* Trends for the response amplitude ( $A$ ) normalised to its maximum value for  $\beta_{\text{exp}} \in [2 \times 10^{-3}, 0.3]$  and  $\nu_{\text{obs}} = 15$  GHz. The blue lines correspond to the case of only adiabatic cooling, and the orange lines to the case of radiative plus adiabatic cooling. *Bottom panel:* Same as in top panel but for  $\nu_{\text{obs}} \in [10, 40]$  GHz and  $\beta_{\text{exp}} = 0.1$ . All the other parameters are the same as reported in Table 2.

the cooling times can produce deviations in the  $t_{\text{decay}}$  trend. We investigate these deviations in Section 5.2.

As a final comment, we investigate the impact of the complex interplay between the cooling timescales on the response function amplitude  $A$ . Even if in the current analysis we are not investigating the dependence of  $A$  on the physical parameters, it is worth showing the impact of the cooling times. In the top panel of Figure 10, we plot the trends for the response amplitude normalised to its maximum value, for  $\beta_{\text{exp}} \in [2 \times 10^{-3}, 0.3]$  and  $\nu_{\text{obs}} = 15$  GHz. The blue lines correspond to the case of only adiabatic cooling, and the orange lines to the case of radiative plus adiabatic cooling. In the bottom panel of the same figure, we plot the trends for  $\nu_{\text{obs}} \in [10, 40]$  GHz and  $\beta_{\text{exp}} = 0.1$ . All the other parameters are the same as reported in Table 2. We notice that changes in  $\beta_{\text{exp}}$  introduce variations of up to one order of magnitude for the case of radiative plus adiabatic cooling, and up to  $\approx 40\%$  for the case of only adiabatic cooling. For the case of  $\nu_{\text{obs}}$  trends, the variation in the response is up to  $\approx 20\%$ , both for only adiabatic and adiabatic plus radiative cooling. Therefore, the response amplitude is also affected mostly by the balance between

radiative and adiabatic cooling, which depends strongly on the expansion velocity.

## 5.2. $\beta_{\text{exp}}$ trends

To investigate how the system responds to changes in  $\beta_{\text{exp}}$ , we use the long-term simulations, with ten different values of  $\beta_{\text{exp}}$  evaluated on a logarithmic grid ranging  $[0.001, 0.3]$ , performing the analysis in the observer frame, and we select the 15 GHz frequency. For each value of  $\beta_{\text{exp}}$ , we find the best fit response from Equation 21, and investigate the trends of the parameters  $\Delta t^{\text{obs}}$ ,  $t_{\text{rise}}^{\text{obs}}$ ,  $t_{\text{decay}}^{\text{obs}}$  with the predictions from Equations 25.

The results for the trends are shown in Figure 11, and the corresponding best-fit values are reported in Table 3. We start from the decay trend (top left panel, orange dashed line). The best-fit value for the parameter  $R_0^{\text{obs}} = (1.7 \pm 0.1) \times 10^{14}$  cm, which corresponds to a blob frame value of  $R_0 \approx 5.2 \times 10^{15}$  cm and is in very good agreement with the value of  $R_0 = 5 \times 10^{15}$  cm used in our simulation. The best-fit estimated value  $\nu_{\text{SSA}}^{0,\text{obs}} = 100 \pm 10$  GHz is compatible within one sigma with the simulation value of 90 GHz. Also, the value of  $m_B$  returned by the delay trend (bottom right panel of Figure 11), we again find values of  $R_0$  and  $\nu_{\text{SSA}}^{0,\text{obs}}$ , close to the simulation values. We are also able to estimate the value of  $t_{\text{exp}}^{\text{obs}} = (3.57 \pm 0.01) \times 10^5$  s with good accuracy, which is an agreement with the actual one within a few percent. Finally, we estimate the electron distribution index  $p$  from the best-fit parameters  $\phi$  and  $m_B$  using the second equation of Equation 8. The estimated values of  $p$  for all the three trends are in a very good agreement with the simulation value of  $p \approx 1.5$ .

For the rising time trend (top right panel of Figure 11), the best fit value of  $R_0^{\text{obs}} = (1.9 \pm 0.5) \times 10^{14}$  cm corresponds to a blob rest-frame value of  $R_0 \approx 5.7 \times 10^{15}$  cm, which is within a  $\approx 15\%$  deviation from the simulated value. The best-fit value of  $\nu_{\text{SSA}}^{0,\text{obs}} = 110 \pm 40$  is compatible with the simulated value of 90 GHz but with a significant dispersion. For the delay trend (bottom right panel of Figure 11), we again find values of  $R_0$  and  $\nu_{\text{SSA}}^{0,\text{obs}}$ , close to the simulation values. We are also able to estimate the value of  $t_{\text{exp}}^{\text{obs}} = (3.57 \pm 0.01) \times 10^5$  s with good accuracy, which is an agreement with the actual one within a few percent. Finally, we estimate the electron distribution index  $p$  from the best-fit parameters  $\phi$  and  $m_B$  using the second equation of Equation 8. The estimated values of  $p$  for all the three trends are in a very good agreement with the simulation value of  $p \approx 1.5$ .

## 5.3. $\nu$ trends

To investigate the trends as a function of  $\nu^{\text{obs}}$ , we use the simulation with  $\beta_{\text{exp}} = 0.1$ , where  $\nu^{\text{obs}}$  is the frequency of the observed radio light curves. We stress that the ratio  $\nu_{\text{SSA}}^0/\nu_{\text{SSA}}^*$  can be expressed using either the *blob* or the *observed* frequencies, because the ratio will cancel out the beaming transformation. We follow the same approach as in Section 5.2, with the only difference being that we use  $\nu$  as an independent variable. The results are shown in Figure 12, and the best-fit results are reported in Table 4. For the decay trend (top left panel), we find  $R_0^{\text{obs}} \approx 1.7 \times 10^{14}$  cm, corresponding to a blob frame value of  $R_0 \approx 5.1 \times 10^{15}$  cm, which is in good agreement with the simulation value. The best-fit value of  $\nu_{\text{SSA}}^{0,\text{obs}} = 100 \pm 20$  GHz is compatible with that measured in the simulated SEDs. Both the estimate

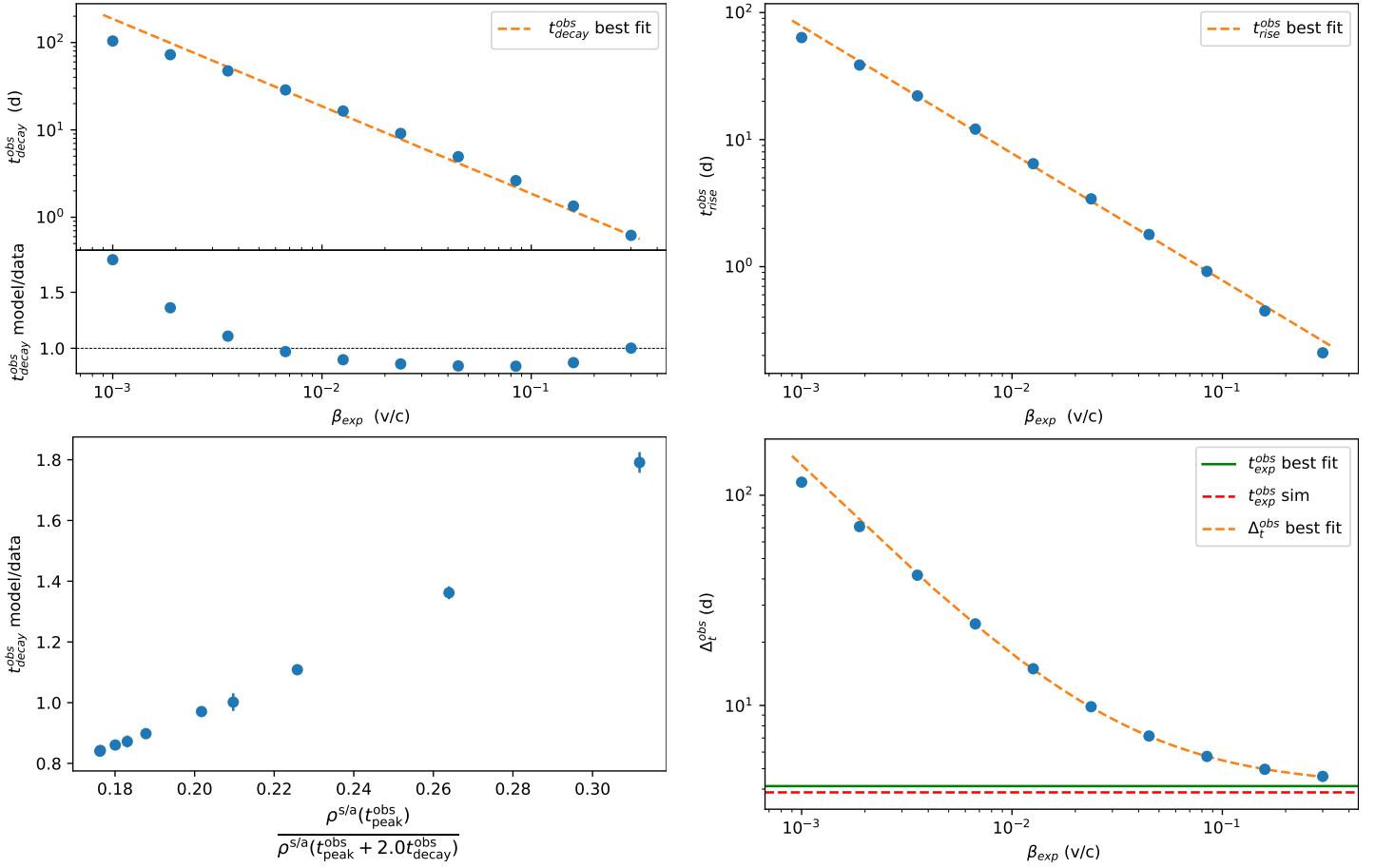


Fig. 11: Expanding trends for  $\beta_{\text{exp}}$  obtained from the simulations. *Top left panel*:  $t_{\text{decay}}^{\text{obs}}$  (blue solid points) obtained from the best fit for the radio- $\gamma$  response for the ten simulations with  $\beta_{\text{exp}}$  ranging [0.001, 0.3]. The dashed line represents the best fit with the first equation of Equation 25. *Top right panel*: Same as in the top left panel, but for the case of  $t_{\text{rise}}^{\text{obs}}$ . The dashed line corresponds to the best fit with the second equation of Equation 25. *Bottom right panel*: Same as in the top left panel, but for  $\Delta t^{\text{obs}}$ . The dashed line corresponds to the best fit with the third equation of Equation 25. *Bottom left panel*: Strong correlation between the fit model-to-data ratios and the cooling ratios in Figure 9.

Table 3: Best-fit results, for the  $\beta_{\text{exp}}$  simulations

		actual values		values from $\beta$ trend best fit		
		blob	obs	$t_{\text{rise}}^{\text{obs}}$	$t_{\text{decay}}^{\text{obs}}$	$\Delta t^{\text{obs}}$
$R_0$	cm	$5 \times 10^{15}$	$1.66 \times 10^{14}$	$(1.9 \pm 0.5) \times 10^{14}$	$(1.7 \pm 0.1) \times 10^{14}$	$(1.8 \pm 0.1) \times 10^{14}$
$\nu_{\text{SSA}}^0$	GHz	3	90	$110 \pm 40$	$100 \pm 10$	$100 \pm 5$
$t_{\text{exp}}$	s	$1 \times 10^7$	$3.3 \times 10^5$			$(3.57 \pm 0.01) \times 10^5$
$m_B$		1			$0.96 \pm 0.06$	
$\phi$				$0.6 \pm 0.1$	$0.52 \pm 0.04$	$0.54 \pm 0.02$
$p$		1.46		$1.6 \pm 0.3$	$1.5 \pm 0.01$	$1.57 \pm 0.05$

**Notes.** Best-fit results, for the  $\beta_{\text{exp}}$  simulations of the trends reported in Equation 25 for  $t_{\text{rise}}^{\text{obs}}$ ,  $t_{\text{decay}}^{\text{obs}}$ , and  $\Delta t^{\text{obs}}$ , and shown in the top left, top right, and bottom left panels of Figure 11, respectively. The parameter  $p$ , i.e. the electron distribution spectral index, is evaluated from the best-fit parameters using the second equation of Equation 8.

of  $\beta_{\text{exp}} = 0.09 \pm 0.01$  and the estimate of  $m_B 1.0 \pm 0.1$  are in excellent agreement with the simulation values. The  $t_{\text{rise}}$  trend (top right panel of Figure 12) returns a value of  $R_0^{\text{obs}} = 2.4 \pm 1.0 \times 10^{14}$ , which is  $\approx 60\%$  larger than the simulation value, but still compatible within one sigma. The  $\beta_{\text{exp}} = 0.03 \pm 0.01$  is significantly lower than the simulated one. The value of  $\nu_{\text{SSA}}^{0,\text{obs}} \approx 90 \pm 10$  provides a very good estimate of the simulation value  $\nu_{\text{SSA}}^{0,\text{obs}} = 90$  GHz, but, as mentioned in the previous section, this value repre-

sents a lower bound. In the top left panel of Figure 12, the green shaded area shows the  $1\text{-}\sigma$  the interval from the best fit, and the vertical red dashed line represents the simulation value. The delay trend (bottom left panel of Figure 12) returns an estimate of  $\beta_{\text{exp}} = 0.06 \pm 0.01$ , which is  $\approx 40\%$  lower than the simulation value, and an estimate of  $\nu_{\text{SSA}}^{0,\text{obs}} \approx 90 \pm 10$  GHz, which is in agreement with the simulation value. In this case, we also estimate the value of  $t_{\text{exp}}^{\text{obs}} = (3.4 \pm 0.1) \times 10^5$  s with good accuracy, which is

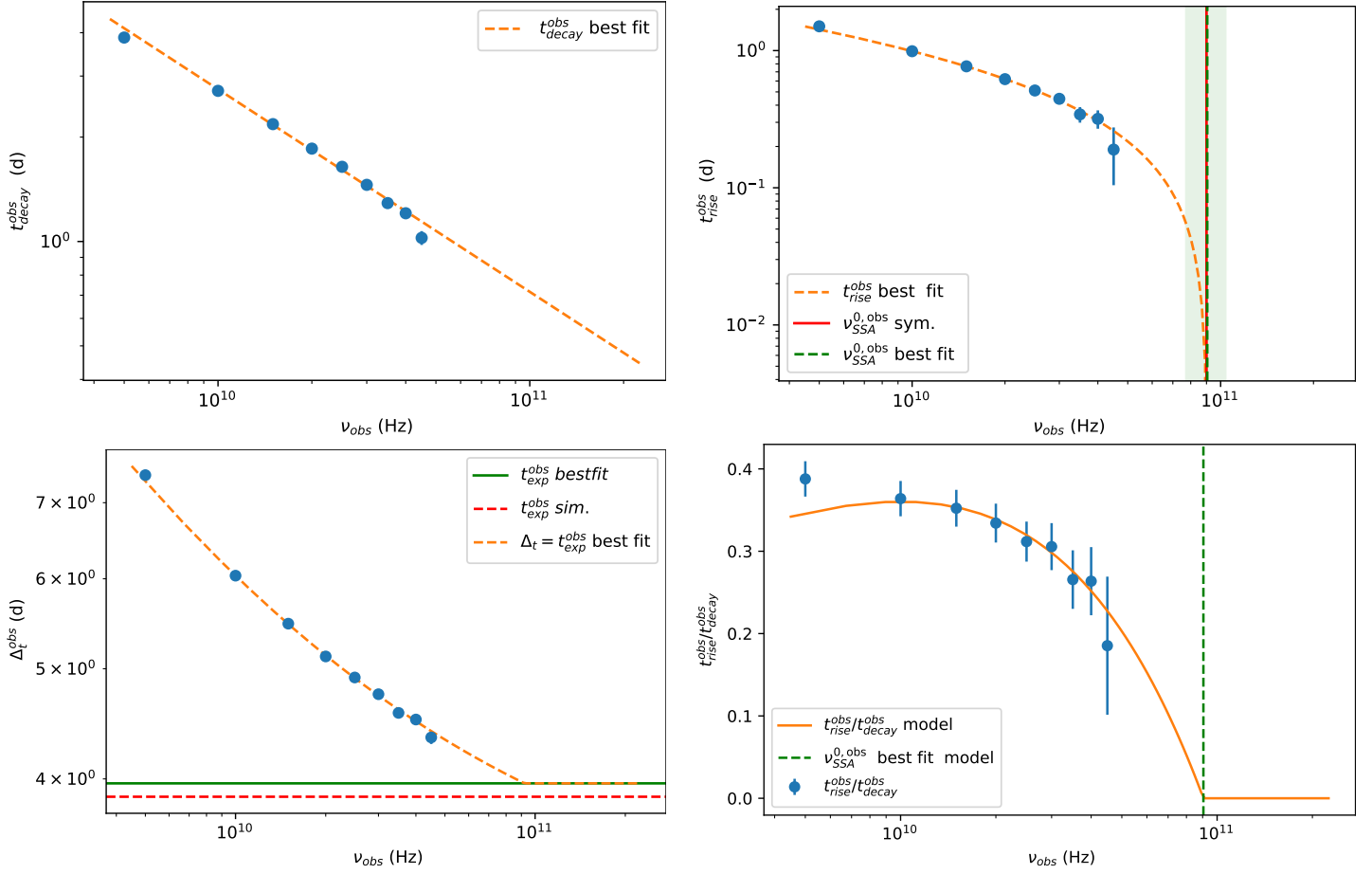


Fig. 12: Expanding trends for  $\nu$  obtained from the simulations. *Top left panel*: Decay times (blue solid points) obtained from the best fit for the radio- $\gamma$  response, for the simulation with  $\beta_{\text{exp}} = 0.1$  and ranging  $\nu_{\text{obs}} = [5, 45]$  GHz. The orange dashed line represents the best fit with first equation of Equation 25. *Top right panel*: Same as in the top left panel, but for the case of  $t_{\text{rise}}^{\text{obs}}$ . The dashed line corresponds to the best fit with the second equation of Equation 25. *Bottom left panel*: Same as in the top left panel, but for  $\Delta t^{\text{obs}}$ . The dashed line corresponds to the best fit with the third equation of Equation 25. *Bottom right panel*: Trend of  $t_{\text{rise}}^{\text{obs}}/t_{\text{decay}}^{\text{obs}}$  as observed in the simulations (solid blue points) compared to the expectation from the individual best-fit trends of  $t_{\text{rise}}^{\text{obs}}$  and  $t_{\text{decay}}^{\text{obs}}$  (dashed line).

Table 4: Best fit results, for the  $\nu_{\text{obs}}$  simulations

		actual values		values from $\nu$ trend best fit		
		blob	obs	$t_{\text{rise}}^{\text{obs}}$	$t_{\text{decay}}^{\text{obs}}$	$\Delta t^{\text{obs}}$
$R_0$	cm	$5 \times 10^{15}$	$1.66 \times 10^{14}$	$(2.4 \pm 1.0) \times 10^{14}$	$(1.7 \pm 0.2) \times 10^{14}$	$(1.6 \pm 0.1) \times 10^{14}$
$\nu_{\text{SSA}}^0$	GHz	3	90	$90 \pm 10$	$100 \pm 20$	$90 \pm 10$
$t_{\text{exp}}$	s	$1 \times 10^7$	$3.3 \times 10^5$			$(3.4 \pm 0.1) \times 10^5$
$m_B$		1			$1.0 \pm 0.1$	
$\beta_{\text{exp}}$	c	0.1		$0.03 \pm 0.01$	$0.09 \pm 0.01$	$0.06 \pm 0.01$
$\phi$				$0.24 \pm 0.07$	$0.58 \pm 0.02$	$0.50 \pm 0.02$
$p$		1.46		$0.6 \pm 0.2$	$1.7 \pm 0.1$	$1.4 \pm 0.1$

**Notes.** Best fit results, for the  $\nu_{\text{obs}}$  simulations, of the trends reported in Equation 25 for  $t_{\text{rise}}^{\text{obs}}$ ,  $t_{\text{decay}}^{\text{obs}}$ , and  $\Delta t^{\text{obs}}$ , and shown in the top left, top right, and bottom left panels of Figure 12, respectively. The parameter  $p$ , i.e. the electron distribution spectral index, is evaluated from the best-fit parameters using the second equation of Equations 8.

in agreement with the simulation value within a few percent. Finally, we comment on the effect of the initial SSA frequency on the rising time. As already noted, the rising time decreases to zero as  $\nu_{\text{SSA}}^*$  approaches  $\nu_{\text{SSA}}^0$ . This implies that even if we obtain a long decay time because of the low expansion rate, we might expect a short rising time if  $\nu_{\text{SSA}}^*$  is close to  $\nu_{\text{SSA}}^0$ . As in

the case of the  $\beta_{\text{exp}}$  trends, we estimate the electron distribution index  $p$  from the best-fit parameters using the second equation of Equation 8. The agreement with the simulation value is lower than in the case of the  $\beta_{\text{exp}}$  trends, in particular for the case of the rise time trend, but nevertheless both delay and decay times

provide an estimate that is consistent within one sigma with the simulation value.

## 6. Comparison with observational data

Here we show how we derive the radio- $\gamma$ -ray response using real data from *Fermi*-LAT (Atwood et al. 2009) and from the OVRO radio telescope (Richards et al. 2011) for three well-known sources. The results are discussed in Sect. 7 in the framework of the model outlined above.

To reconstruct the radio light curve, we convolved the GeV light curve with the response profile given by Eq. 21 and optimised the response parameters to obtain a match with the observed radio data. The response is based on a single flare profile, even if the radio light curves consist of many overlapping consecutive flares in addition to a background flux. As, in reality, the response parameters might change from flare to flare, the response we derive should be considered as an average, possibly driven by the most prominent flares. As a consequence, short-term features, such as spiky structures, could be smoothed and suppressed. The main aim of this section is to show that the physical mechanism investigated in the previous section is responsible for the systematic delayed radio emission, and to understand whether or not these average timescales are compatible with those predicted by the model, assuming physical parameters within the range of those used in the simulations

Delayed responses were already observed by Max-Moerbeck et al. (2014) for specific flares of Mrk 421 and Mrk 501 and interpreted as the propagation of shocks through conical jets. The same interpretation was proposed (Türler et al. 1999) to explain the long-term light curves of 3C 273, and in particular the radio flares corresponding to overlapping stretched and delayed GeV flares (Esposito et al. 2015).

The results indicated below show that a constant response profile is adequate for Mrk 421 and Mrk 501, while the response amplitude appears variable from flare to flare in the case of 3C 273. We also find that the background flux could be considered as constant in Mrk 421 and Mrk 501, possibly accounting for the core emission, while it is slowly variable and firmly associated to the jet in 3C 273.

### 6.1. Data

The Large Area Telescope on board the Fermi Gamma-ray Space Telescope (*Fermi*-LAT) is the most sensitive  $\gamma$ -ray telescope in the 20 MeV  $< E < 300$  GeV energy range. *Fermi*-LAT uses a charged particle tracker and a calorimeter to detect photons. The point spread function (PSF) depends on energy, reaching a  $1\sigma$ -equivalent containment radius of  $\sim 0.1^\circ$  at 40 GeV (Atwood et al. 2009). Despite *Fermi*-LAT being sensitive to  $\gamma$ -rays of about 20 MeV, because of the energy-dependent PSF we can only reliably consider photons with energies between 100 MeV and 300 GeV. Data reduction was performed using the PASS8 pipeline and the Fermi Science Tool v10r0p5 package. Sources from the *Fermi*-LAT four-year point-source catalogue were used for the fitting model. More details on the performed analysis can be found in Arbet-Engels et al. (2021a). Because of their different  $\gamma$ -ray fluxes, we used different time bins for each source: 3 days, 1 day, and 7 days for 3C 273, Mrk 421, and Mrk 501, respectively. In the case of Mrk 501, we also reduced the considered energy range to 1-300 GeV leading to a reduction in the flux uncertainties thanks to the better PSF and a lower background in that energy range.

Regular radio observations of Mrk 421, Mrk 501, and 3C 273 were performed at 15 GHz by the 40 m radio telescope of the Owens Valley Radio Observatory (OVRO) (Richards et al. 2011). These observations were conducted as part of the *Fermi* blazars monitoring campaign. The light curves (with twice-per-week cadence) were publicly available (when we started the analysis) from the OVRO archive<sup>3</sup>. We removed all the data points with a significance of less than  $5\sigma$ , because these observations were performed during unfavourable observing conditions.

### 6.2. Mrk 421

The radio light curve of Mrk 421 is broadly correlated to the GeV light curve, with radio lagging behind the GeV variations by 30–100 days at the maximum of the discrete correlation function (Arbet-Engels et al. 2021a).

The best-fit response was obtained by minimising, over a 7.5-year period (MJD 55500–58226), the deviations between the observed radio light curve and the synthetic light curve obtained by the convolution of the Fermi LAT daily binned light curve with a response (Eq. 21). The Fermi LAT light curve starts about two years before the period used for the minimisation to account for the long-lasting effect of the response, particularly  $\Delta t$ .

The observed GeV and radio and the resulting synthetic radio light curves are shown in Fig. 13, and the best-fit parameters are listed in Table 5. The uncertainties on the synthetic light curve were derived using direct uncertainty propagation from the Fermi LAT light curve and response profile through the convolution with the response profile. The best-fit synthetic light curve is similar, but does not perfectly match the observed radio light curve, possibly indicating that the intensity of the response (e.g. the constant A) might be variable with time. Also, a fast radio flare near MJD 56897 and a wider flare at about MJD 55600 (see Fig. 13) could not be reproduced. These flares could have a different origin or may need a different response (such adjustments were also used by Esposito et al. 2015, and could indicate different conditions in various shocks). As the uncertainties on the GeV light curve and on the response profile are not Gaussian nor independent, the goodness of fit ( $\chi^2/\nu = 1243/218 = 5.9$ ) between the observed and synthetic radio data is only indicative. As the response rise time is similar to the binning time of the GeV light curve, its value indicates a rising time of shorter than one day.

### 6.3. Mrk 501

The correlation between the GeV and radio light curves is also strong in Mrk 501 with radio variations lagging behind the GeV

<sup>3</sup> <http://www.astro.caltech.edu/ovroblazars/>

Table 5: Best-fit parameters for the  $\gamma$ -ray to radio response profile for Mrk 421.

Parameter	Value
A	$12.5^{+0.5}_{-0.013} \times 10^3$ Jy cm <sup>2</sup> s/ph
$t_{rise}$	$\lesssim 1$ day
$t_{decay}$	$126.5^{+1.3}_{-1.3}$ days
$\Delta t$	$37.58^{+0.13}_{-0.13}$ days
$F_{background}$	$0.18^{+0.008}_{-0.0004}$ Jy

**Notes.** Best-fit parameters for the  $\gamma$ -ray to radio response profile (Eq. 21) with the addition of a background radio flux.

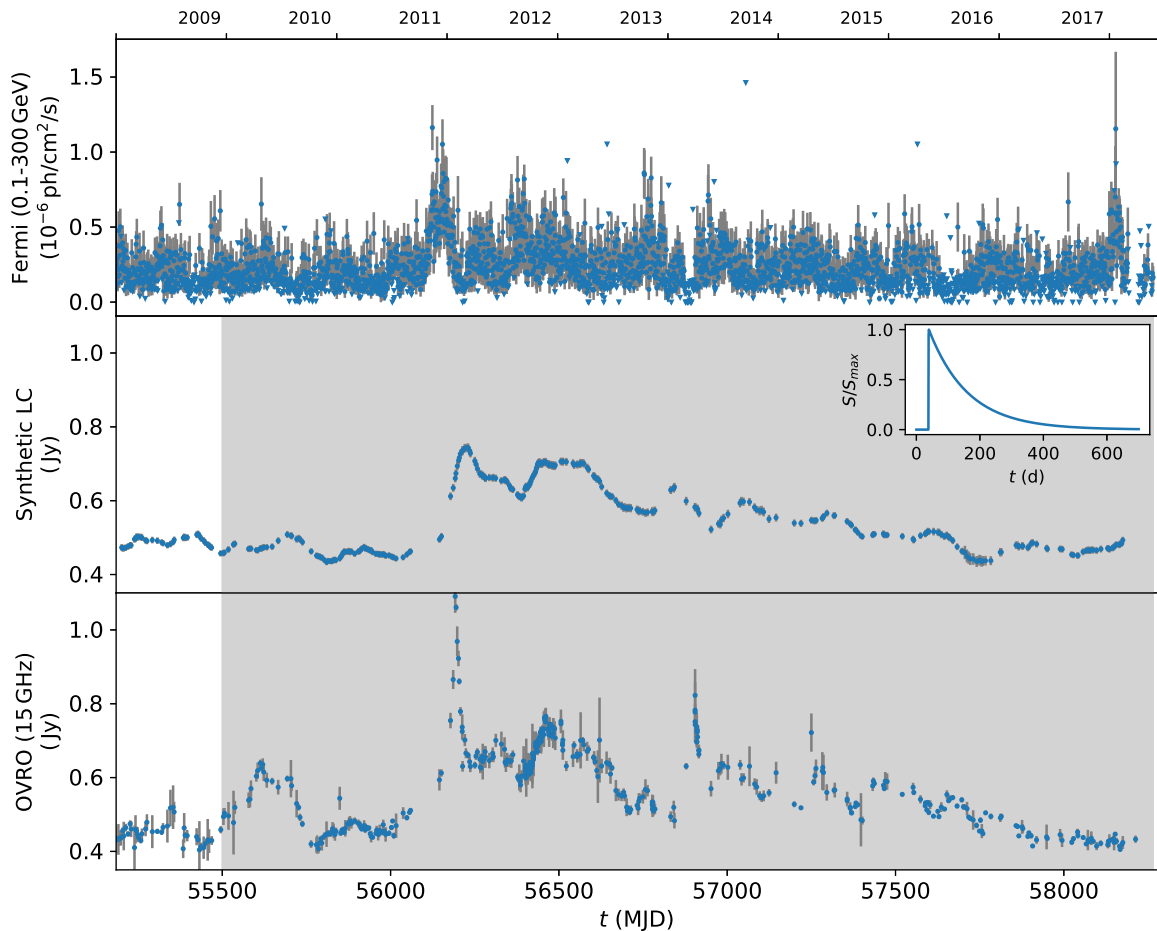


Fig. 13: Synthetic radio light curve for Mrk 421 (middle) created as a convolution of the day-binned Fermi-LAT 0.1-300 GeV light curve (top) and of the radio response (inset panel), compared with the OVRO 15 GHz radio light curve (bottom). Fitting time range is highlighted in grey.

ones by 170-250 days (Arbet-Engels et al. 2021b). To further probe the connection between these bands, we searched for the delayed response profile, which, when convolved with the GeV light curve, can mimic the radio variations.

Adopting the analytical response profile defined by Eq. 21 together with a constant background emission ( $\sim 0.9$  Jy) and minimising the deviations between the observed and synthetic radio data ( $\chi^2/\nu = 258/112 = 2.3$ ) led to a best-fit response decaying in 66 days after a delay of about 224 days as displayed in Fig. 14 (inset panel) and parametrised in Table 6. The minimisation was performed for the period starting on MJD 56800, because prior to that the GeV-radio correlation is weak, indicating that additional noise or emission components are present.

Table 6: Best-fit parameters for the  $\gamma$ -ray-to-radio response for Mrk 501.

Parameter	Value
$A$	$166_{-3}^{+5} \times 10^4$ Jy cm <sup>2</sup> s/ph
$t_{rise}$	$12_{-4}^{+4}$ days
$t_{decay}$	$73_{-3.6}^{+3.6}$ days
$\Delta t$	$234_{-10}^{+10}$ days
$F_{background}$	$0.915_{-0.004}^{+0.004}$ Jy

**Notes.** Best-fit parameters for the  $\gamma$ -ray-to-radio response profile (Eq. 21) with the addition of a background radio flux.

#### 6.4. 3C 273

The GeV-radio response for the FSRQ 3C 273 was investigated and discussed in Esposito et al. (2015) using light curves lasting for about 6 years. The radio data could be reproduced using a convolution of the GeV light curve through a response profile varying only in amplitude from flare to flare.

We performed a similar analysis including additional data and found that for 3C 273 a single response profile cannot reproduce the complete radio light curve, unlike for Mrk 421 and Mrk 501. The addition of a slowly changing background radio emission was required, which was estimated with a third-order Savitzky-Golay filter of the observed radio emission with a windows size of 501 days, which is long enough to prevent fitting of individual radio flares (dotted line in Fig. 15). This variable background component needs to be bright (about 90% of the total emission) and cannot be accounted for by the core emission of 3C 273. This emission is linked to the jet itself. The variability of that component cannot be well constrained.

Figure 15 shows the original *Fermi*-LAT and radio light curves, and the synthetic radio light curve derived as described above. We had to adjust the amplitude of the response for different individual flaring periods while the other response parameters could remain unchanged, as found by Esposito et al. (2015). The response profile (best-fit parameters listed in Table 7) was derived using a single flare ( $\gamma$ -ray time range [54710, 54890] MJD) with a goodness of fit  $\chi^2/\nu = 88.5/59 = 1.5$ . The ampli-

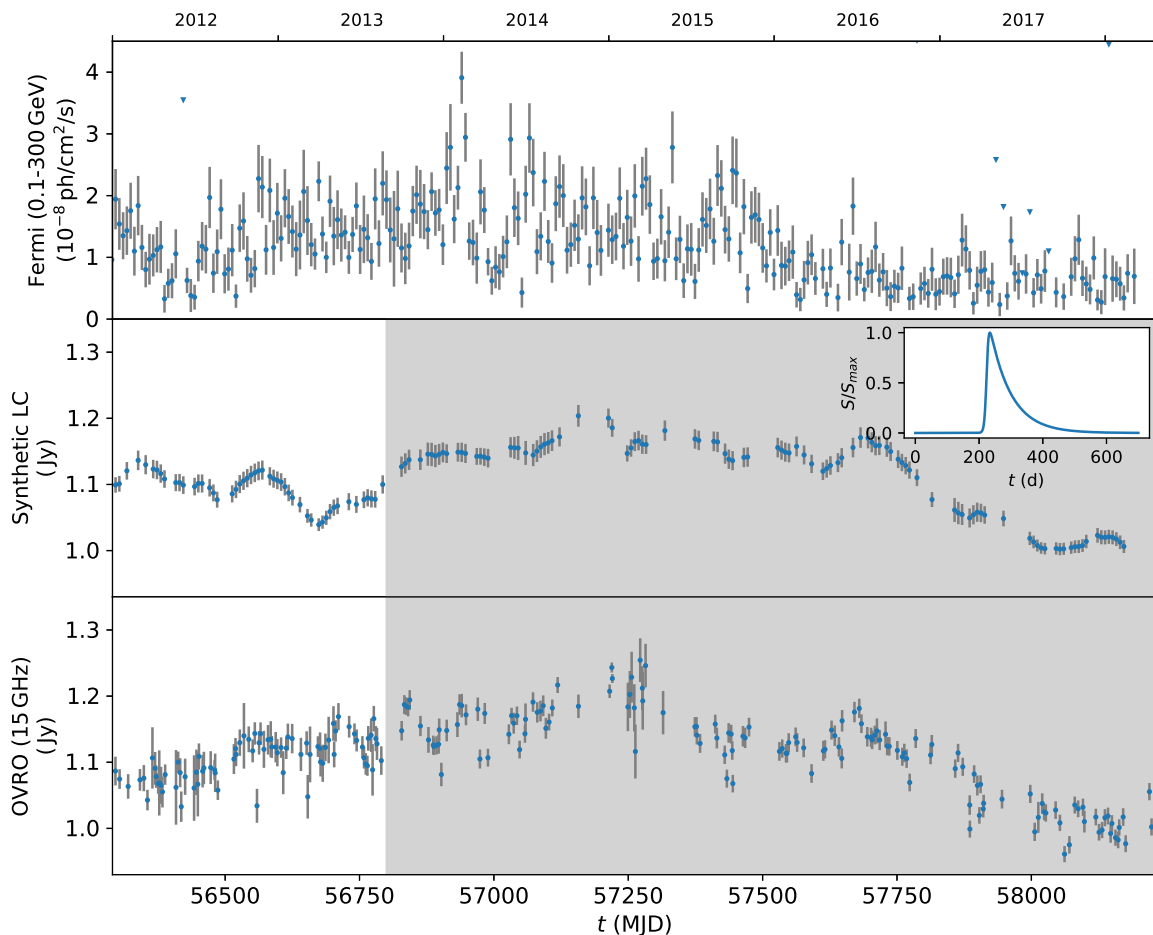


Fig. 14: Mrk 501 synthetic radio light curve (middle), created as a convolution of the weekly binned Fermi-LAT 1-300 GeV light curve (top) and of the radio response (inset of the middle panel), compared with the OVRO 15 GHz radio light curve (bottom). The fitting time range is highlighted in grey.

tudes of the response for the individual flaring periods (listed in Tab. 8) were determined on the full range of radio observations. The variations of the response amplitude during different flares can be explained by two possible factors:

- A transition from a SSC- to an external Compton (EC)-dominated IC emission regime. Indeed, the amplitude of the response strongly depends on the initial radiative output of both the IC and S components at the flaring state. Hence, a different contribution from the EC emission can impact the response amplitude.
- As shown in Section 5, and in particular in Figure 10, there is a strong effect of the competition between synchrotron and adiabatic cooling times on the modulation of the response amplitude. In particular, we notice that, for changes in  $\beta_{\text{exp}}$ , variations on the response amplitude of up to one order of magnitude are possible, whilst for changes in  $\nu_{\text{obs}}$  the variations can be up to 40%. As for 3C 373, the modulation of the amplitude ranges from  $\approx 0.5$  to  $\approx 5$  (see Table 8), we can assume that the observed modulation can also be explained as a change in  $\beta_{\text{exp}}$ . Moreover, a change in the EC contribution can impact the radiative-adiabatic balance, producing effects similar to those produced by changes in  $\beta_{\text{exp}}$ .

We also note that the slowly changing background (dotted line in the middle and bottom panels of Figure 15) needed for the radio emission does not affect the  $\gamma$ -ray component. This

discrepancy seems to be unrelated to the EC/SSC transition, because the radio- $\gamma$  response reproduces the detrended radio light curves. A possible explanation could be provided by a change in the baseline of the radio emission at the expansion site, possibly related to a change in the beaming factor and therefore related to the jet-blob geometry. In any case, the fact that the modulated baseline alone allows us to reproduce the trend suggests that the physical cause of the modulation is not affecting the physical mechanism of the response.

Table 7: Best-fit parameters of the  $\gamma$ -ray(*Fermi*-LAT)-to-radio response profile for 3C 273.

Parameter	Value
$A_0$	$174^{+12}_{-11} \times 10^3 \text{ Jy cm}^2 \text{ s/ph}$
$t_{\text{rise}}$	$37^{+2}_{-2} \text{ days}$
$t_{\text{decay}}$	$69^{+3}_{-3} \text{ days}$
$\Delta t$	$276^{+10}_{-10} \text{ days}$

**Notes.** Best-fit parameters of the  $\gamma$ -ray(*Fermi*-LAT)-to-radio response profile (see Eq. 21).

## 7. Discussion

The results presented in the present analysis provide a self-consistent framework with which to explain the observed delay

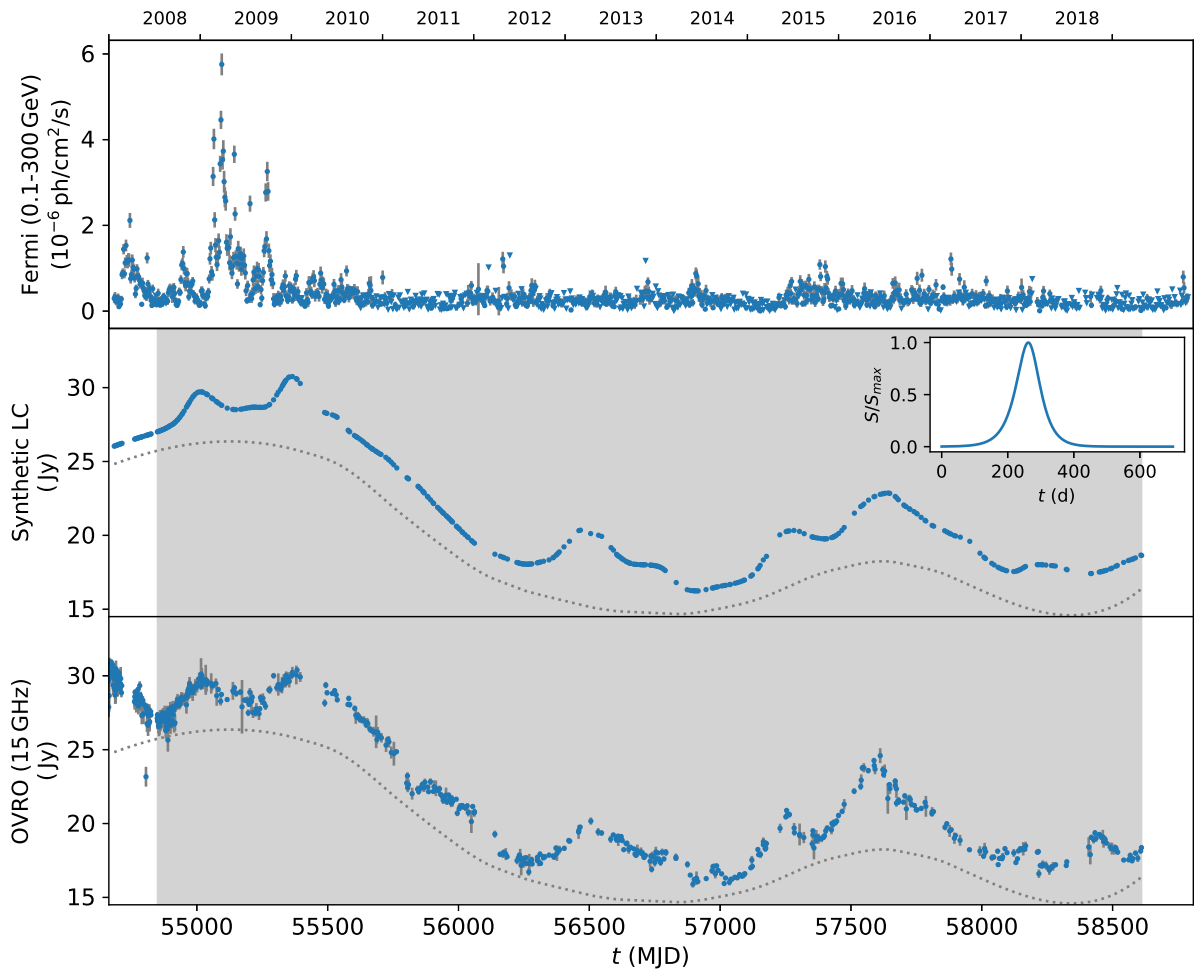


Fig. 15: 3C 273 synthetic radio light curve (middle), created as a convolution of the 3-days-binned Fermi-LAT 0.1-300 GeV light curve (top) and of the radio response (inset panel), compared with the OVRO 15 GHz radio light curve (bottom). Amplitude fitting time range is highlighted in grey. The shape of the response profile (Table 7) was determined using the  $\gamma$ -ray flaring period 54710 - 54890 MJD. The dotted line shows a slowly varying background radio flux, which cannot be reproduced by the response convolution approach. The response amplitude was adjusted for different time intervals.

Table 8: Response amplitude multiplicative factor for different flaring periods of 3C 273.

Period, MJD	Value
54684-54890	$1.07 \pm 0.11$
54890-55340	$0.69 \pm 0.04$
55340-56125	$1.39 \pm 0.08$
56125-56530	$5.31 \pm 0.16$
56530-56920	$0.46 \pm 0.15$
56920-57250	$5.3 \pm 0.4$
57250-57710	$2.71 \pm 0.12$
57710-57910	$0.88 \pm 0.17$
57910-58110	$3.5 \pm 0.3$
58110-58610	$2.4 \pm 0.3$

in the radio emission with respect to the  $\gamma$ -ray activity observed in several blazars. The development of a flaring episode, followed taking into account radiative and acceleration processes, results in an initial self-absorption frequency of above  $10^{11}$  Hz (according to our initial setup), and therefore the radio delay will occur under the hypothesis of an expanding blob when the source size is large enough to move the SSA at frequencies comparable to or lower than the observed radio light curve. The particles

need to be confined in order to observe a delayed peak in the radio light curve. In our analysis, we decoupled the acceleration region from the radiative region, and this is why escape timescales acting in the radiative region do not impact the accelerated electrons. Moreover, because of the expansion, it is natural to expect the escape time of the particles to increase.

Similar analyses and comparable results have been presented by Boula et al. (2018) and Potter (2018) but only a qualitative comparison could be performed with our results as these latter works did not present a quantitative analysis of the delays or the phenomenological relations linking the delay to the physical parameters of the jet, and assume an arbitrary electron distribution in the flaring region. The time lags versus the expansion velocity presented in Boula et al. (2018) follows a similar trend to that reported in the bottom left panel of Figure 11, with a delay going asymptotically to  $\Delta t = 0$ , as predicted by our model and confirmed by our simulations. The time lags versus the initial source size  $R_0$  (Fig. 3 of Boula et al. 2018) is the result of the change in the SSA frequency with the source size and can therefore be compared with our result shown in the bottom left panel of Figure 12. Potter (2018) used a large-scale parabolic to conical jet structure in qualitative agreement with our results. Even if the agreement with these models can only be qualitative —because

the analyses were performed with different methods and numerical codes (Potter 2018; Boula et al. 2018)—, the comparison provides orthogonal checks, the results of which appear to support the hypothesis of an expanding blob related to the radio- $\gamma$  connection in blazars.

One of the main novelties of our analysis, and one that is missing in previous studies, is the determination of the single flare response, and its verification via a self-consistent numerical model, taking into account both acceleration and radiation process, and the determination of the phenomenological relations that link not only the delay but also the rise and decay time to the expansion velocity, magnetic field index, and initial SSA frequency. The proposed single-flare response is able to reproduce the radio light curve as a convolution of the  $\gamma$ -ray light curve, and we verified that the timescales of the response follow the phenomenological trends. This allowed us to establish a link between some physical parameters, such as the emitting region initial size,  $R_0$ , the jet magnetic field index  $m_B$ , and the observed response. In particular, the derivation of the initial source size can provide an orthogonal method compared to the determination based on MW SED fitting or variability timescales.

We also investigated other effects of the adiabatic expansion. In particular, we analysed the impact on the CD, verifying that as the source size increases, the consequent decrease in photon and electron density leads to a drop in the CD. This effect, if present at the time of the flare ( $t_{\text{exp}} = 0$ ), can provide a hint for the blob expansion before the observation of the radio delay. It is extremely interesting that, very recently, MAGIC Collaboration et al. (2021) presented an analysis of the correlation patterns of Mrk 421 in 2017, finding that adiabatic expansion without significant particle losses can be invoked to explain the pattern of the CD evolution. The authors also verified that the adiabatic cooling timescales should be longer than those necessary to explain a cooling break compatible with their MW data, requiring adiabatic timescales of the order of weeks to months in the observer frame that are in good agreement with our proposed scenario. Moreover, the authors also state that the expanding blob can explain  $\gamma$ -ray orphan flares. The scenario proposed in MAGIC Collaboration et al. (2021) is highly compatible with our scenario, as we can set  $t_{\text{exp}} = 0$  without any loss of generality, and proves that, for Mrk 421, both the radio delay and the CD effect are confirmed by the data. Also, comparisons with the data shown in Section 6 indicate that our model can accurately reproduce the radio light curve as a response to the  $\gamma$ -ray light curve over a time-span of years, and the relevant timescales derived from the response function are in agreement with those derived from the self-consistent modelling. In particular, for Mrk 421, the analysis in Section 6.2 returns a best-fit value of  $\Delta_t \approx 37$  days with a decay time of  $\approx 126$  days, which corresponds to  $\beta_{\text{exp}} \lesssim 0.01$  (see Sect. 5.2). The value of the decay time, which according to our model is a proxy for the adiabatic cooling time, is also in nice agreement with the decay time of the order of weeks to months reported in MAGIC Collaboration et al. (2021).

To get a deeper understanding of the physics embedded in the convolution analysis, we used a MCMC approach using the `emcee`<sup>4</sup> package (Foreman-Mackey et al. 2013). We define a composite log-likelihood  $\mathcal{L} = \mathcal{L}_{\text{rise}} + \mathcal{L}_{\text{decay}} + \mathcal{L}_{\text{delay}}$ , where  $\mathcal{L}_{\text{rise}}$ ,  $\mathcal{L}_{\text{decay}}$ , and  $\mathcal{L}_{\text{delay}}$  represent the log-likelihood functions corresponding to rise, decay, and delay time in Equation 25. Each likelihood is evaluated assuming that the parameters returned by the convolution analysis are distributed according to a Gaussian

PDF:

$$\mathcal{L} \propto \sum_{i=[1,2,3]} -\frac{1}{2} \frac{(x_i - \mu_i)^2}{2\sigma_i^2} - \frac{1}{2} \ln(\sigma_i^2), \quad (26)$$

where  $\mu_i$  and  $\sigma_i$  represent best-fit parameter values and the  $1-\sigma$  errors, respectively, for  $\Delta_t$ ,  $t_{\text{rise}}^{\text{obs}}$ , and  $t_{\text{decay}}^{\text{obs}}$  obtained in the convolution analysis, and  $x_i$  represents the corresponding parameter evaluated from Equation 25. In order to sample the parameter space, we ran a chain with  $10^4$  steps, and a burn-in length of 1000 steps, checking that the chain was always converging. We use uninformative flat priors, with  $m_B \in [1, 2]$ ,  $\phi \in [1/3, 1]$ ,  $\nu_{\text{SSA}}^{0,\text{obs}} \in [10, 10^4]$  GHz,  $\beta_{\text{exp}} \in [10^{-4}, 1]$ . To determine the range on  $R_0^{\text{obs}}$ , we started from setting a flat range for the observed  $\gamma$ -ray variability timescale  $t_{\gamma}^{\text{var}} \in [0.25, 14]$  days, and we set  $R_0^{\text{obs}} = t_{\gamma}^{\text{var}} c$ , leading to  $R_0^{\text{obs}} \in [6.5 \times 10^{13}, 3.6 \times 10^{17}]$  cm. As the phenomenological relations have a bias with respect to the case where radiative cooling is taken into account (see Section 5, Figure 7) we add 5% systematic error to the convolution analysis results. In Appendix C we provide a validation of the method against the simulation for  $\beta_{\text{exp}} = 0.1$ . In Figures 16, 17, and 18, we plot the posterior contour maps (where the solid black line identifies the  $1-\sigma$  containment for a bivariate Gaussian distribution). On the diagonal, we plot the marginalised posterior distributions. The blue vertical line in the  $\log(\nu_{\text{SSA}}^{0,\text{obs}})$  histogram identifies the 15 GHz observed OVRO frequency. In figure 19, we plot the histogram of the values of the electron distribution index  $p$  obtained from the posterior values of  $m_B$  and  $\phi$ , and using the second equation of Equation 8. We notice that the MCMC is able to provide informative confidence regions for the parameters of interest, except for  $\log(R_0)$  estimated for Mrk 421, where we notice a flat posterior for  $\log(R_0^{\text{obs}}) = 15.67^{+0.59}_{-0.59}$ . In all the other cases, we get informative posteriors. The magnetic index, for Mrk 421,  $m_B = 1.39^{+0.38}_{-0.29}$  has the peak of the PDF at  $m_B = 1$ . For the same source, we notice the low value of  $\log(\nu_{\text{SSA}}^{0,\text{obs}}) = 10.34^{+0.09}_{-0.06}$ , corresponding to  $\nu_{\text{SSA}}^{0,\text{obs}} \approx 22$  GHz, driven by the short  $t_{\text{rise}}^{\text{obs}}$  returned by the convolution analysis, and very close the observed OVRO frequency of 15 GHz. For the case of Mrk 501, we obtain  $\log(R_0^{\text{obs}}) = 15.60^{+0.60}_{-0.54}$ ,  $m_B = 1.31^{+0.36}_{0.22}$ . In this case, the PDF is also peaking at  $m_B \approx 1.0$ . The initial SSA frequency  $\log(\nu_{\text{SSA}}^{0,\text{obs}}) = 11.26^{+0.84}_{-0.49}$ , which is larger than in the case of Mrk5 421, is compatible with the longer rise time. Regarding 3C 273, we obtain  $\log(R_0^{\text{obs}}) = 15.53^{+0.61}_{-0.50}$ ,  $m_B = 1.48^{+0.28}_{-0.18}$ , but in this case the PDF is not peaking at  $m_B = 1$ . In this case, as in the case of Mrk 501, we also obtain a larger value of  $\log(\nu_{\text{SSA}}^{0,\text{obs}}) = 11.69^{+0.76}_{-0.61}$  compared to the case of Mrk 421. Regarding the index  $\phi$ , we find it interesting to discuss the estimate on the electron index  $p$ . Indeed, as  $\phi$  plays the same role as  $\psi$ , we can use the second equation of Equation 8 to estimate the posterior distribution of  $p$  from the posterior values of  $m_B$  and  $\phi$ . The result is shown in Figure 19. For the case of Mrk 421, we find a confidence level of  $p = 1.97^{+1.26}_{-0.72}$ , for Mrk 501  $p = 2.00^{+1.14}_{-0.73}$ , and for 3C 273  $p = 2.27^{+1.18}_{-0.84}$ . The value of 3C 273 is compatible with a stronger cooling regime, and is therefore in agreement with the presence of an EC radiative component. For all the objects, the values of  $p$  are compatible with the predictions from Fermi first-order acceleration plus a stochastic component, which is in agreement with previous theoretical and observational analyses (Tramacere et al. 2009; Tramacere et al. 2011).

Nevertheless, the convolution analysis performed with the observed data can be affected by numerous sources of bias; in particular, our use of a single response for the full time-span, encompassing several flaring episodes, with the possibility that the

<sup>4</sup> <https://emcee.readthedocs.io/en/stable/>

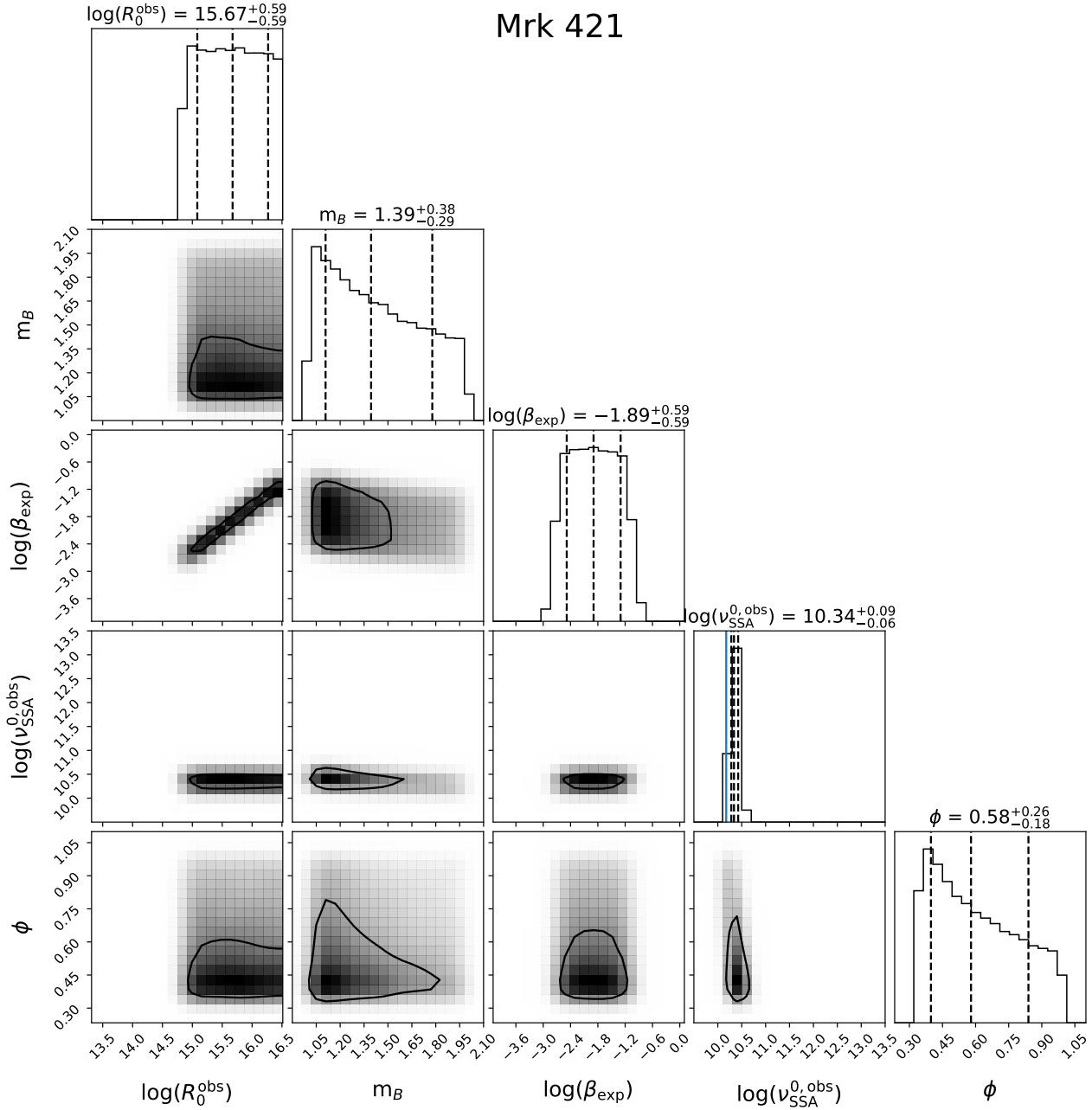


Fig. 16: Posterior distribution for a MCMC sampling of the composite log-likelihood reported in Equation 26 for rise, decay, and delay time in Equation 25. To sample the parameter space, we use uninformative flat priors, with  $m_B \in [1, 2]$ ,  $\phi \in [1/3, 1]$ ,  $\nu_{SSA}^{0,obs} \in [10, 10^4]$  GHz,  $\beta_{exp} \in [10^{-4}, 1]$ . The range of  $R_0^{obs}$  is determined by setting a flat range for the observed  $\gamma$ -ray variability timescale  $t_{\gamma}^{var} \in [0.25, 14]$  days, and setting  $R_0^{obs} = t_{\gamma}^{var} c$ , corresponding to  $R_0^{obs} \in [6.5 \times 10^{13}, 3.6 \times 10^{17}]$  cm. We plot the posterior contour maps (where the solid black identifies the  $1-\sigma$  containment for a bivariate Gaussian distribution). On the diagonal, we plot the marginalised posterior distributions, and with the vertical dashed black lines we indicate the 0.16, 0.5, and 0.84 quantiles. The blue vertical line in the  $\log(\nu_{SSA}^{0,obs})$  histogram identifies the 15 GHz observed OVRO frequency. On top of each marginalised histogram we report the confidence level corresponding to the quantiles.

response from flare to flare might change due to different physical conditions in each single flare. There are further effects that we do not take into account in the present work and that can have an impact:

- Changes in the Bulk Lorentz factor, or in the magnetic index  $m_B$ . These effects might actually be connected, and could lead to deviations in the trends presented in the previous section. For example, a decrease in the Bulk Lorentz factor after the beginning of the expansion would produce observed de-

cay times that are significantly longer than those derived in the blob frame.

- External photon fields can impact the response amplitude, and indeed the evolution of the radio flare if the EC field is dominant at the scale where the expansion takes place. In this latter case, we would expect a lower response amplitude compared to the case of pure SSC. Moreover, the transition from SSC- to EC-dominated regimes can impact the competition between the adiabatic and radiative timescales, with

## Mrk 501

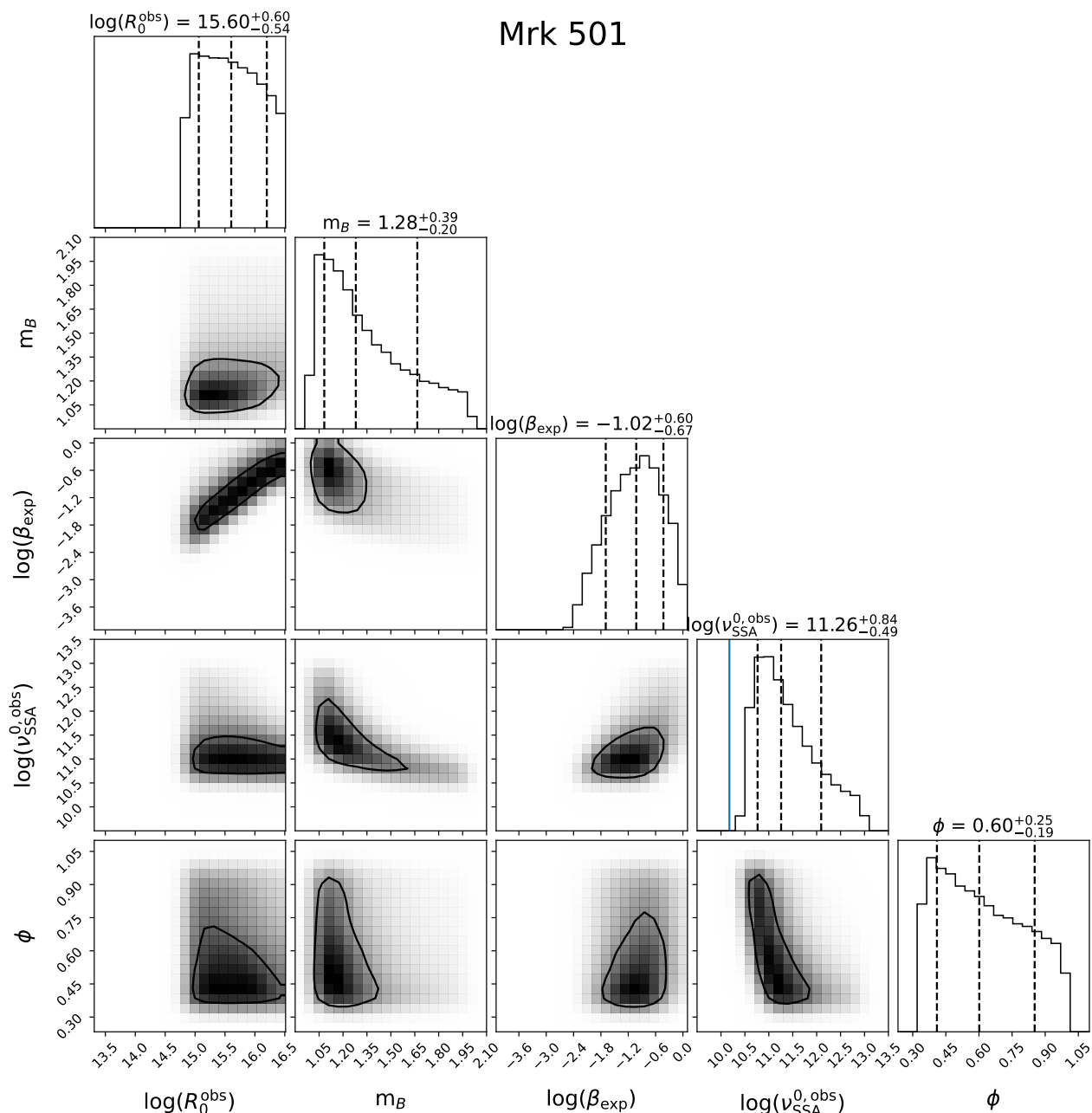


Fig. 17: Same as in Figure 16, but for the case of Mrk 501.

effects similar to those investigated in the case of the synchrotron cooling.

- A further bias is introduced by the sampling of the IC window for different classes of objects. For example, in the case of FSRQs, the Fermi window (0.1-300 GeV) is sampling the EC bump close to the SED peak, whilst in the case of HBLs, Fermi is sampling the rising part of the IC bump. We therefore expect a different dynamics in the light curves.
- Regarding the interplay between escape times and source size, because particle escape time is  $\propto R/c$ , we could expect significant escape at the time of the flare, with increasing escape times as long as the source expands. This, again, might lead to modulation of the amplitude and also the SSA frequency. The combination of these effects could impact the slopes of the trends in Equation 25
- In general, changes to the initial SSA frequency,  $v_{\text{SSA}}^{0,\text{obs}}$ , related to different combinations of  $N^{\text{tot}}$  and  $B_0$  will lead to the

same trends as those in Equation 25. Given the functional form of the term  $(v_{\text{SSA}}^{0,\text{obs}}/v_{\text{SSA}}^{*,\text{obs}})^\phi$ , these trends with respect to  $v_{\text{SSA}}^{*,\text{obs}}$  will have a changed sign in the exponent.

Nevertheless, the agreement between the observed radio data and the results obtained from the convolution with a single response is satisfactory and supports the hypothesis that adiabatic expansion is the main driver of the observed radio delay. It is interesting to note a possible connection between the expansion and the polarisation measurements. According to Yusef-Zadeh et al. (2007), for an expanding blob, the polarisation rotation measure (RM) follows the trend  $RM \propto NRB$ , which for our setup (constant  $N(t)R^3(t)$ ), will scale as  $RM \propto R^{-3}$  for  $m_B = 1$ , and as  $RM \propto R^{-4}$  for  $m_B = 2$ . Therefore, in the case of an expansion we expect the RM to decrease at lower radio frequencies, and would

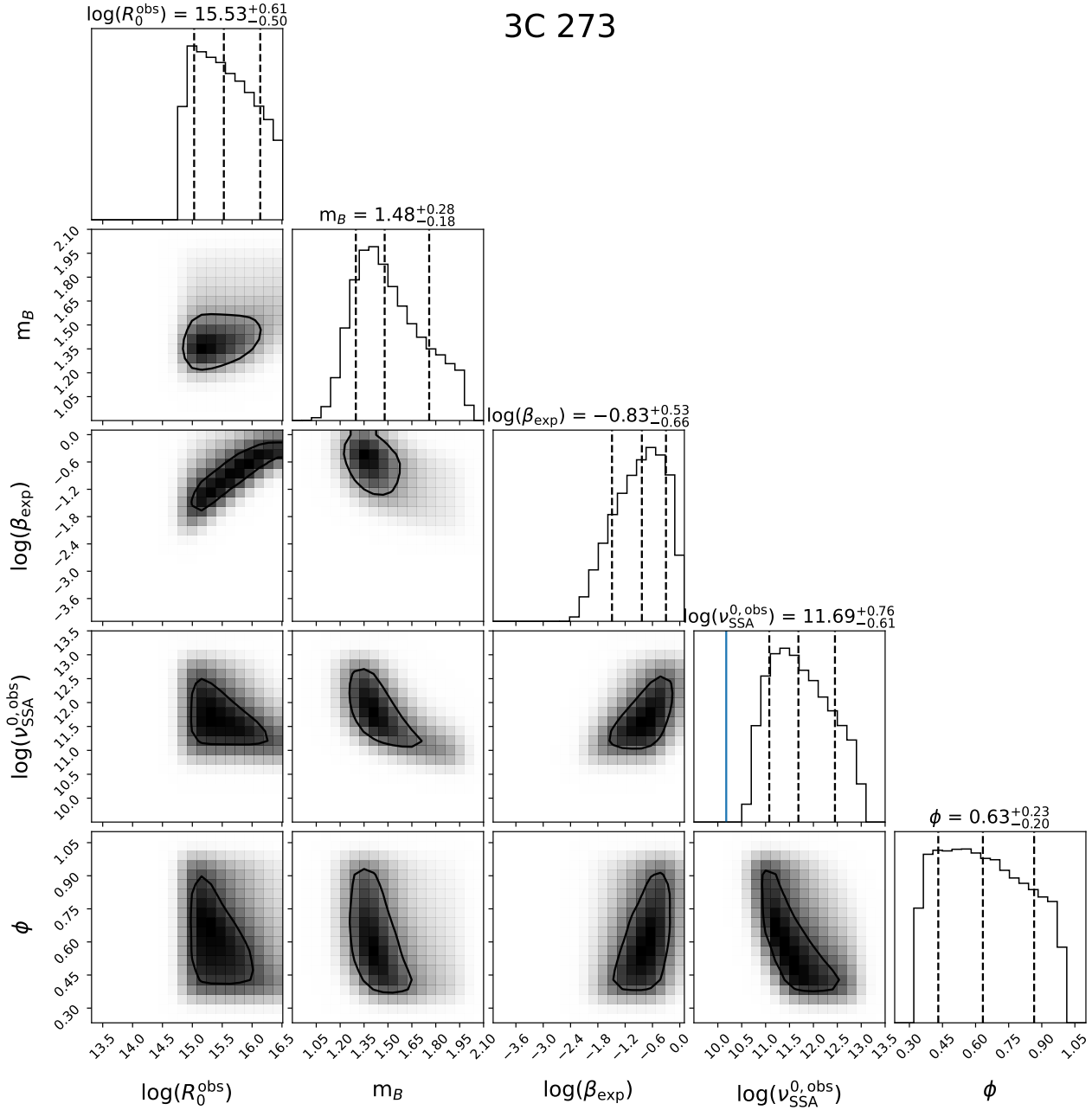


Fig. 18: Same as in Figure 16, but for the case of Mrk 3C 273.

also expect a correlation between the RM polarisation and the radio light curves.

We note that the change in the SSA frequency with time, and the consequent delay, might also be related to a bending jet. Indeed, the SSA frequency will change according to the observing angle for a slab geometry, as discussed by Ghisellini et al. (1985). In this case, we would expect a change of the beaming factor, and also a shift of the SSA frequency (to higher values if the bending results in a lower synchrotron optical thickness). Therefore, if the bending orientates the shorter side of the slab towards the line of sight of the observer, a further delay is to be expected. On the contrary, if the rotation orientates the larger side of the slab toward the line of sight of the observer, no additional delay should be observed. We can provide a rough estimate of the distance travelled by the emitting region during the observed delay using Equation 17, which for  $\delta\Gamma \approx 100$  and

$\beta_\Gamma \approx 1$  would result in  $\Delta_r$  of the order of  $3 \times 10^{12} \frac{\Delta_{\text{obs}}}{\text{ls}}$  cm, that is of the order of  $10^{18-19}$  cm for observed delays of the order of a few weeks to months. During this timescale, the jets should bend towards the observer in such a way as to move the SSA frequency down to the GHz window. We should also consider that the total amount of requested rotation will also depend on the slab aspect ratio, and that, for a square aspect ratio, we would expect almost no delay. We notice that a rotation towards the line of sight of the observer would also result in a larger beaming factor compared to initial one observed during the  $\gamma$ -ray flaring episode, adding an extra achromatic variability pattern induced by the change in the beaming factor. All these effects make it difficult to understand the extent to which bending alone, that is, without expansion, could explain the observed delays. Nevertheless, it is possible that both processes happen, and therefore

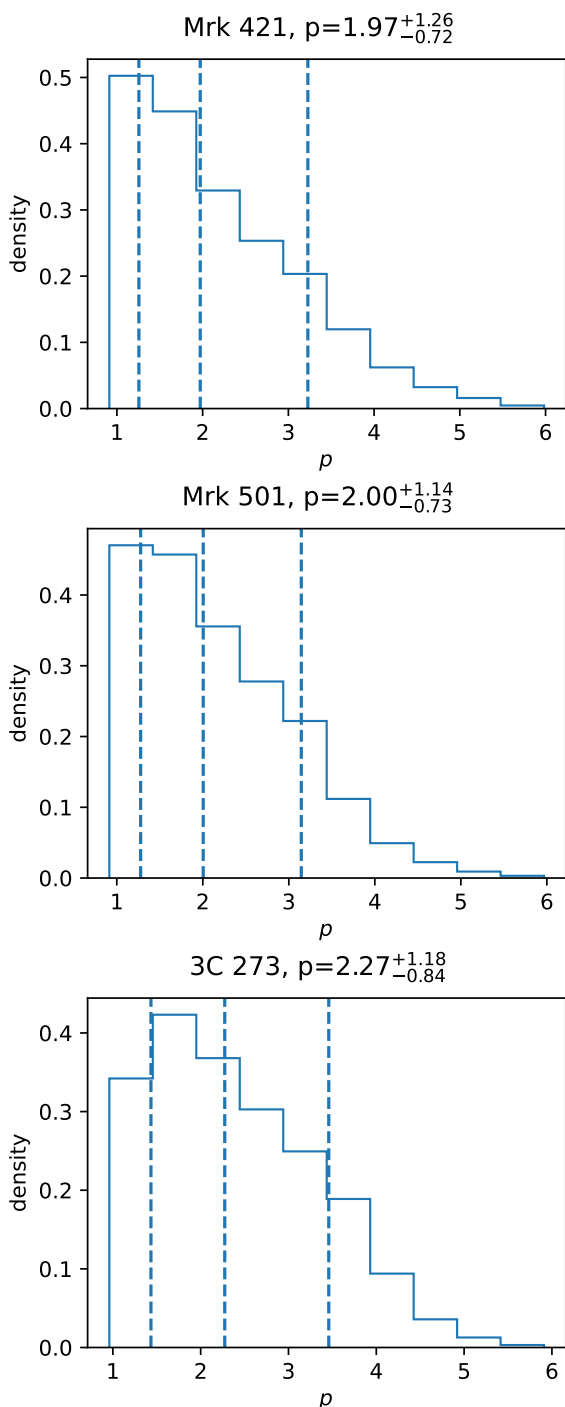


Fig. 19: Posterior distributions of the electron distribution index  $p$  obtained from the posterior of  $m_B$  and  $\phi$  returned by the MCMC sampler. *Top panel:* Mrk 421, *middle panel:* Mrk 501, *Bottom panel:* 3C273.

it would be interesting to look for unambiguous signatures, such as an achromatic variability pattern.

We might speculate that, in agreement with the conclusions presented in Kovalev et al. (2020), the place where the  $\gamma$ -ray flare occurs is upstream of or close to the parabolic-to-conical transition site, and should provide ideal conditions for shock formation or for magnetic reconnection, which could lead to first- and second-order particle acceleration, both included in our model. A  $\gamma$ -ray flaring region at parsec scale is easily compatible with

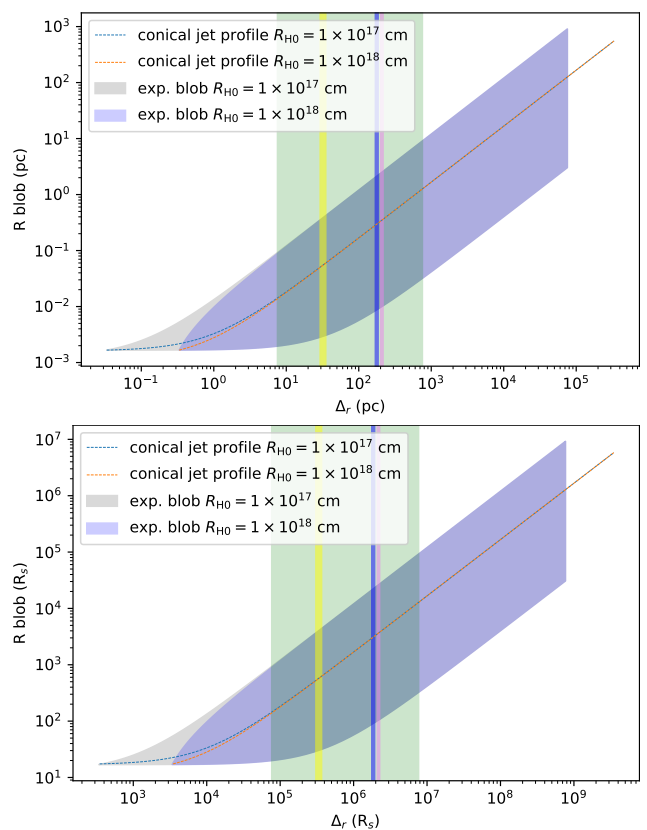


Fig. 20: *Top Panel:* Evolution of blob size ( $R$ ), versus distance travelled by the blob across the jet ( $\Delta_r$ ). The grey shaded area represents the evolution of  $R$  for a blob expanding with constant velocity, with a range of  $\beta_{\text{exp}} = [0.001 - 0.3]$ , for a Bulk Lorentz factor of 25, an observing angle of 1.5 deg,  $t_{\text{exp}} = 0$ ,  $R_0 = 5 \times 10^{15}$  cm, and  $R_{H0} = 1 \times 10^{17}$  cm. The green shaded area represents the corresponding  $\Delta_r$  interval for a range of observed delay of  $\Delta_t^{\text{obs}} = [10, 1000]$  days. The blue shaded area represents the same trend for the case of  $R_{H0} = 1 \times 10^{18}$  cm.  $R_{H0}$  is the site of the  $\gamma$ -ray flare. The blue dashed line represents a conical jet profile for  $R_{H0} = 1 \times 10^{17}$  cm and the orange dashed line for  $R_{H0} = 1 \times 10^{18}$  cm, both starting from an initial value of  $R_0 = 5 \times 10^{15}$  cm. The yellow, blue, and purple shaded regions represent the  $\Delta_t^{\text{obs}}$  for Mrk 421, Mrk 501, and 3C273, respectively. *Bottom Panel:* Same as in the left panel, replacing the spatial units with the Schwarzschild radius for a BH mass of  $10^9 M_{\odot}$ .

our analysis. In the top panel of figure 20, we plot (grey shaded area) the evolution of  $R$ , i.e. the blob size, versus  $\Delta_r$ , the distance travelled by the blob across the jet, for a constant expansion velocity, with a range of  $\beta_{\text{exp}} = [0.001 - 0.3]$ , for a Bulk Lorentz factor of 25, and an observing angle of 1.5 deg. We also set  $t_{\text{exp}} = 0$ ,  $R_0 = 5 \times 10^{15}$  cm, and  $R_{H0} = 1 \times 10^{17}$  cm. We notice that for all three sources in our analysis, we find an estimate of  $\Delta_r$  above 10 pc. For the case of Mrk 421,  $\Delta_r \approx 30$  pc, and for both Mrk 501 and 3C 237,  $\Delta_r$  is above  $\approx 100$  pc. The estimate  $\Delta_r$  is particularly relevant for FSRQs. Indeed, Costamante et al. (2018) found that, due to the lack of broad line region (BLR) absorption features in the Fermi-LAT spectra of 106 FSRQs, the site of the  $\gamma$ -ray emission has to be placed beyond the BLR. For the case of Fermi-LAT FSRQs, assuming an average disk luminosity of  $L_d \approx 1.5 \times 10^{46}$  erg  $s^{-1}$ , and a radius of the BLR given by  $R_{\text{BLR}} = 10^{17} L_{d,45}^{1/2}$  (Ghisellini et al. 2010), the expected av-

erage value for  $R_{\text{BLR}}$  is  $\approx 4 \times 10^{17}$  cm. For the case of 3C273, where we find a delay of  $\approx 276$  days, and the disk luminosity is  $L_{\text{d}} \approx 5 \times 10^{46}$  erg s $^{-1}$ , the corresponding value of the BLR size is  $R_{\text{BLR}} \approx 7 \times 10^{17}$  cm ( $\approx 0.23$  pc). Hence, our estimate for 3C 273 of  $\Delta_r \gtrsim 100$  pc for  $0.001 < \beta_{\text{exp}} < 0.3$  is compatible with a  $\gamma$ -ray site beyond the BLR, in agreement with the analysis in Costamante et al. (2018). We conclude that the scales inferred from the radio delays analysis are in agreement with those returned by the analysis of the radio jet profiles, with the jet showing a conical profile above  $\sim [1-10]$  pc, and with the  $\gamma$ -ray emission happening beyond the BLR in FSRQs.

Finally, the fact that we can reproduce the radio light curve as a response to the  $\gamma$ -ray light curve over long-term timescales and with a single response has several implications. First, we notice that this might suggest a quite stable configuration of the expansion process, and also that the expansion is persistent along with the other physical mechanisms responsible for the flaring activity. Also, we notice that this could disfavour the possibility of lepto-hadronic emission, at least as a persistent mechanism. Indeed, in lepto-hadronic models, the core of the  $\gamma$ -ray emission is due to the proton synchrotron, whilst the synchrotron bump is mainly of leptonic origin (Zech et al. 2017). This would lead to an almost uncorrelated variability in the synchrotron and in the IC component, making it almost impossible to reproduce the radio light curve with a single response to the  $\gamma$ -ray emission.

## 8. Conclusions

In this work, we present a fully self-consistent numerical and phenomenological framework that incorporates a response function and a physical model of the relevant timescales. We use this framework to explain the radio and  $\gamma$ -ray responses and delays observed in the long-term light curves of several blazars. We implemented a self-consistent simulation to reproduce the radio- $\gamma$  delays using the `JetSeT` code. In this first approach, we focused our analysis on the derivation of phenomenological trends and consequent verification with numerical simulations. Our main goals are to identify the main physical drivers of the delay, and to derive and validate a response function able to reproduce the delayed radio flare as a response to the  $\gamma$ -ray flare. We used a basic simple assumption of a single blob moving with a bulk Lorentz factor  $\Gamma$  and constant expansion velocity  $\beta_{\text{exp}}$ . The main findings of our analysis can be summarised as follows:

- From our phenomenological relations, we predict that the delay of the radio emission occurs at a lower frequency than the initial SSA frequency, with an off-set given by the time interval between the flaring episode  $t_{\text{exp}}$ , which without any loss of generality can be set to zero.
- Our phenomenological trends, summarised in Equation 14, also suggest that both rise and decay times are inversely proportional to  $\beta_{\text{exp}}$  and are directly proportional to the distance in frequency between the initial SSA frequency and the frequency at which the radio-delayed light curve is observed. Moreover, as the magnetic field is bound to the size of the emitting region through the magnetic index  $m_B \in [1, 2]$  by Equation 2, we also predict an inverse proportionality between the decay time and  $m_B$ .
- We set up our simulations in order to follow the trends with respect to both  $\beta_{\text{exp}}$  and the frequency of the radio light curves. We estimated the relevant timescales using the best-fit results of the convolution of the response function given in Equation 21, applied to the simulated  $\gamma$ -ray and radio light

curves. We verified that the delayed light curves are reproduced with excellent accuracy by the convolution of the  $\gamma$ -ray light curve with the proposed response function.

- We also verified that the phenomenological trends given by Equation 25 are in very good agreement with the simulations when the adiabatic cooling is dominant, and we evaluated the deviations when the radiative cooling is competing. By fitting these trends to the estimated parameters of response functions, we are able to recover the relevant input parameters of the simulations, such as the initial size of the emitting region ( $R_0$ ), the initial SSA frequency,  $\beta_{\text{exp}}$ , and  $m_B$ . This proves that it is possible to derive parameters connected to the jet and magnetic field topology from MW long-term campaigns.
- We also verified that when the expansion is active, a sudden drop in the Compton dominance is observed, and therefore investigating the time profile of the IC emission during the flaring episode could provide information on whether or not there is an expansion starting during the flare.
- We applied our model to observations of the two HBLs, Mrk 421 and Mrk 501, and the FSRQ 3C 273. First, we verified that a single radio- $\gamma$  response accurately reproduces the long-trend radio light curves, even though short-term features are smoothed out. Then, by means of an MCMC approach that combines the phenomenological trends and the output of the convolution analysis, we are able to estimate the source size, the initial SSA,  $m_B$ , and the electron distribution index  $p$  for these sources, finding satisfactory agreement between the proposed scenario and the observed phenomenology in the literature.
- We compared our results with other results in the literature (Boula et al. 2018; Potter 2018) finding a qualitative agreement, even though the setup of our simulation is not fully equivalent to those used elsewhere. We also verified that recent results presented in MAGIC Collaboration et al. (2021) regarding the correlation patterns of Mrk 421 in 2017 require a framework based on adiabatic expansion with confined emitters, confirming that the expansion can occur as early as the  $\gamma$ -ray flaring episode, and providing further validation of expansion as the mechanism responsible for the radio- $\gamma$  delay.
- We instigated possible applications and predictions of our analysis. In particular, we find that the limit on the initial size of the emitting region derived from the delay analysis is in agreement with typical values returned from MW SED fitting. We discuss the possible implications in terms of polarisation measurements, predicting a correlation between the RM of the polarisation and the radio light curves, with the RM decreasing at lower frequencies.
- We find that the blob expansion presented in our model and constrained from the observed radio responses ( $\beta_{\text{exp}} < 0.3$ ) predicts a conical jet profile at the scale above  $\approx [1-10]$  pc in agreement with the results presented in Kovalev et al. (2020). This is compatible with the hypothesis that the expansion begins when the jets become plasma dominated, a condition that is ideal for the formation of the shock. Hence, the  $\gamma$ -ray flare can be used as a signature of the shock formation, indicating the onset of the jet expansion, i.e. the transition from parabolic to conical profiles, and the radio delay is an indicator of the expansion velocity, and consequently of the jet collimation profile beyond the shock.
- Finally, we find that the strong correlation between the radio and  $\gamma$ -ray emission predicted by our model casts doubt on a lepto-hadronic mechanism, at least as a persistent process acting in the core of blazar jets.

We hope to further extend this work, expanding the parameter space of the current analysis, exploring the impact of variable bulk Lorentz factors, and  $m_B$ , and investigating potential observational signatures of their interconnection by linking these parameters to different jet profiles. We also plan to investigate the role of the light-crossing time as a function of the jet observing angle, and the impact of the EC on the adiabatic–radiative interplay. The code and the analysis presented in this paper are publicly available and fully reproducible (see Appendix A).

*Acknowledgements.* This research has made use of data from the OVRO 40-m monitoring program (Richards et al. 2011), supported by private funding from the California Institute of Technology and the Max Planck Institute for Radio Astronomy, and by NASA grants NNX08AW31G, NNX11A043G, and NNX14AQ89G and NSF grants AST-0808050 and AST-1109911. The following open source codes have been used: Numpy Harris et al. (2020), Scipy Virtanen et al. (2020), Matplotlib Hunter (2007), JetSeT Tramacere (2020); Tramacere et al. (2011); Tramacere et al. (2009), emcee Foreman-Mackey et al. (2013). The authors thank the anonymous referee for the useful and helpful comments on the manuscript.

Richards, J. L., Max-Moerbeck, W., Pavlidou, V., et al. 2011, *ApJS*, 194, 29  
 Rybicki, G. B. & Lightman, A. P. 1986, *Radiative Processes in Astrophysics*  
 Sliusar, V., Arbet-Engels, A., Baack, D., et al. 2019a, in *High Energy Phenomena in Relativistic Outflows VII*, 32  
 Sliusar, V., Arbet-Engels, A., Baack, D., et al. 2019b, in *International Cosmic Ray Conference*, Vol. 36, 36th International Cosmic Ray Conference (ICRC2019), 796  
 Stawarz, Ł. & Petrosian, V. 2008, *ApJ*, 681, 1725  
 Tramacere, A. 2020, *JetSeT: Numerical modeling and SED fitting tool for relativistic jets*  
 Tramacere, A., Giommi, P., Perri, M., Verrecchia, F., & Tosti, G. 2009, *A&A*, 501, 879  
 Tramacere, A., Massaro, E., & Taylor, A. M. 2011, *The Astrophysical Journal*, 739, 66  
 Türler, M., Courvoisier, T. J.-L., & Paltani, S. 1999, *A&A*, 349, 45  
 Ulrich, M.-H., Maraschi, L., & Urry, C. M. 1997, *ARA&A*, 35, 445  
 van der Laan, H. 1969, in *Quasars and high-energy astronomy*, 49  
 Virtanen, P., Gommers, R., Oliphant, T. E., et al. 2020, *Nature Methods*, 17, 261  
 Yusef-Zadeh, F., Wardle, M., Cotton, W. D., Heinke, C. O., & Roberts, D. A. 2007, *ApJ*, 668, L47  
 Zacharias, M. 2021, *Physics*, 3, 1098  
 Zech, A., Cerruti, M., & Mazin, D. 2017, *A&A*, 602, A25

## References

Arbet-Engels, A., Baack, D., Balbo, M., et al. 2021a, *A&A*, 647, A88  
 Arbet-Engels, A., Baack, D., Balbo, M., et al. 2021b, *A&A*, 655, A93  
 Atwood, W. B., Abdo, A. A., Ackermann, M., et al. 2009, *ApJ*, 697, 1071  
 Becker, P. A., Le, T., & Dermer, C. D. 2006, *The Astrophysical Journal*, 647, 539  
 Begelman, M. C., Blandford, R. D., & Rees, M. J. 1984, *Rev. Mod. Phys.*, 56, 255  
 Blandford, R. D. & Königl, A. 1979, *ApJ*, 232, 34  
 Blandford, R. D. & Levinson, A. 1995, *ApJ*, 441, 79  
 Blandford, R. D. & Rees, M. J. 1978, in *BL Lac Objects*, ed. A. M. Wolfe, 328–341  
 Böttcher, M., Reimer, A., Sweeney, K., & Prakash, A. 2013, *ApJ*, 768, 54  
 Boula, S., Petropoulou, M., & Mastichiadis, A. 2018, *Galaxies*, 7, 3  
 Boula, S. & Mastichiadis, A. 2022, *A&A*, 657, A20  
 Brown, L. M. J., Robson, E. I., Gear, W. K., et al. 1989, *ApJ*, 340, 129  
 Chang, J. S. & Cooper, G. 1970, *Journal of Computational Physics*, 6, 1  
 Costamante, L., Cutini, S., Tosti, G., Antolini, E., & Tramacere, A. 2018, *MNRAS*, 477, 4749  
 Esposito, V., Walter, R., Jean, P., et al. 2015, *A&A*, 576, A122  
 Foreman-Mackey, D., Hogg, D. W., Lang, D., & Goodman, J. 2013, *PASP*, 125, 306  
 Ghisellini, G. 2013, *Lecture Notes in Physics*, Vol. 873, *Radiative Processes in High Energy Astrophysics* (Heidelberg: Springer International Publishing)  
 Ghisellini, G., Maraschi, L., & Treves, A. 1985, *A&A*, 146, 204  
 Ghisellini, G., Tavecchio, F., Foschini, L., et al. 2010, *MNRAS*, 402, 497  
 Gould, R. J. 1975, *The Astrophysical Journal*, 196, 689  
 Harris, C. R., Millman, K. J., van der Walt, S. J., et al. 2020, *Nature*, 585, 357–362  
 Hovatta, T., Petropoulou, M., Richards, J. L., et al. 2015, *MNRAS*, 448, 3121  
 Hunter, J. D. 2007, *Computing in Science Engineering*, 9, 90  
 Jones, F. C. 1968, *Physical Review*, 167, 1159  
 Kaiser, C. R. 2006, *MNRAS*, 367, 1083  
 Kardashev, N. S. 1962, *Soviet Ast.*, 6, 317  
 Katarzyński, K., Ghisellini, G., Mastichiadis, A., Tavecchio, F., & Maraschi, L. 2006, *A&A*, 453, 47  
 Kovalev, Y. Y., Pushkarev, A. B., Nokhrina, E. E., et al. 2020, *MNRAS*, 495, 3576  
 Longair, M. S. 2010, *High Energy Astrophysics* (Cambridge: Cambridge University Press), 888  
 MAGIC Collaboration, Acciari, V. A., Ansoldi, S., et al. 2021, *arXiv e-prints*, arXiv:2106.05516  
 Max-Moerbeck, W., Hovatta, T., Richards, J. L., et al. 2014, *MNRAS*, 445, 428  
 McCray, R. 1969, *ApJ*, 156, 329  
 Melrose, D. B. 1969, *Ap&SS*, 5, 131  
 Moderski, R., Sikora, M., Coppi, P. S., & Aharonian, F. 2005, *Monthly Notices of the Royal Astronomical Society*, 363, 954  
 Park, B. T. & Petrosian, V. 1996, *Astrophysical Journal Supplement v.103*, 103, 255  
 Pian, E., Urry, C. M., Maraschi, L., et al. 1999, *ApJ*, 521, 112  
 Potter, W. J. 2018, *MNRAS*, 473, 4107  
 Pushkarev, A. B., Kovalev, Y. Y., & Lister, M. L. 2010, *ApJ*, 722, L7  
 Ramaty, R. 1979, In: *Particle acceleration mechanisms in astrophysics; Proceedings of the Workshop*, 56, 135, a&AA ID. AAA027.078.006  
 Rani, B., Krichbaum, T. P., Marscher, A. P., et al. 2014, *A&A*, 571, L2

## Appendix A: Code availability and reproducibility

The work presented here is fully reproducible by following the instructions in the git repository<sup>5</sup>. In this repository you can find the notebooks to reproduce the analysis and the instructions to install the JetSeT version 1.2.0rc11. We remind the reader that this is a pre-release of the forthcoming 1.2.0 JetSeT version. Further details on the JetSeT code can be obtained by contacting the author Andrea Tramacere (e-mail: [andrea.tramacere@gmail.com](mailto:andrea.tramacere@gmail.com)).

## Appendix B: JetSeT temporal evolution

In the following, we give a detailed description of the cooling terms used in the numerical solution of the FP equation:

$$|\dot{\gamma}_{\text{synch}}(t)| = \frac{4\sigma_{TC}}{3m_e c^2} \gamma^2 U_B(t) = C_0 \gamma^2 U_B(t) \quad (\text{B.1})$$

$$\begin{aligned} |\dot{\gamma}_{IC}(t)| &= \frac{4\sigma_{TC}}{3m_e c^2} \gamma^2 \int f_{KN}(4\gamma\epsilon_0) \epsilon_0 n_{ph}(\epsilon_0, t) d\epsilon_0 \\ &= C_0 \gamma^2 F_{KN}(\gamma, t) \end{aligned} \quad (\text{B.2})$$

$$|\dot{\gamma}_{ad}(t)| = \frac{1}{3} \frac{\dot{V}}{V} \gamma = \frac{\dot{R}(t)}{R(t)} \gamma = \frac{\beta_{\text{exp}} c}{R(t)} \gamma$$

$$C(\gamma, t) = |\dot{\gamma}_{\text{synch}}(t)| + |\dot{\gamma}_{IC}(t)| + |\dot{\gamma}_{ad}(t)|$$

where  $U_B = B^2/8\pi$ , is the energy density of the magnetic field,  $\epsilon_0 = h\nu_0/m_e c^2$  is the IC seed photon energy in units of  $m_e c^2$ , and  $n_{ph}(\epsilon_0)$  is the number density of IC seed photons with the corresponding photon energy density  $U_{ph} = m_e c^2 \int \epsilon_0 n_{ph}(\epsilon_0) d\epsilon_0$ . The function  $f_{KN}$  results from the analytical integration of the Jones (1968) Compton kernel, fully taking into account Klein-Nishina (KN) effects for an isotropic seed photon field (see Moderski et al. 2005, appendix C), and  $F_{KN}(\gamma)$  represents its convolution with the seed photon field. We note that  $F_{KN}$  plays a crucial role in the cooling process, depending both on the IC regime (Thomson (TH) limit for  $4\gamma\epsilon_0 \ll 1$ , KN limit for  $4\gamma\epsilon_0 \gg 1$ ), and on  $\epsilon_0 n_{ph}(\epsilon_0) \propto B^2/R^2$ . The acceleration terms in Eq. 18, and their related timescales, can be expressed as a power-law in terms of the Lorentz factor ( $\gamma$ ):

$$\begin{cases} D_p(\gamma) = D_{p0} \left(\frac{\gamma}{\gamma_0}\right)^q, & t_D = \frac{1}{D_{p0}} \left(\frac{\gamma}{\gamma_0}\right)^{2-q} \\ D_A(\gamma) = 2D_{p0} \left(\frac{\gamma}{\gamma_0}\right)^{q-1}, & t_{DA} = \frac{1}{2D_{p0}} \left(\frac{\gamma}{\gamma_0}\right)^{2-q} \\ A(\gamma) = A_{p0} \gamma, & t_A = \frac{1}{A_0}. \end{cases} \quad (\text{B.3})$$

## Appendix C: MCMC analysis validation

In this section we validate the MCMC analysis presented in Section 8 using as a benchmark the long-term simulations for  $\beta_{\text{exp}} = 0.1$ . We use the same configuration as in the case of the analysis presented in Section 8. In Figure C.1, we plot the MCMC results, and with a vertical red dashed line we report the ‘true’ simulation values. We notice that, in all cases except  $m_B$ , the simulation value is contained within the  $1-\sigma$  confidence range returned by the MCMC posterior. For the case of  $m_B$ , we notice that peak of the posterior PDF matches the simulation value of  $m_B = 1$ . In Figure C.2, we show the same check for the electron distribution index  $p$ . Also in this case, the agreement is excellent.

<sup>5</sup> [https://github.com/andreatramacere/adiabatic\\_exp\\_radio\\_gamma\\_delay](https://github.com/andreatramacere/adiabatic_exp_radio_gamma_delay)

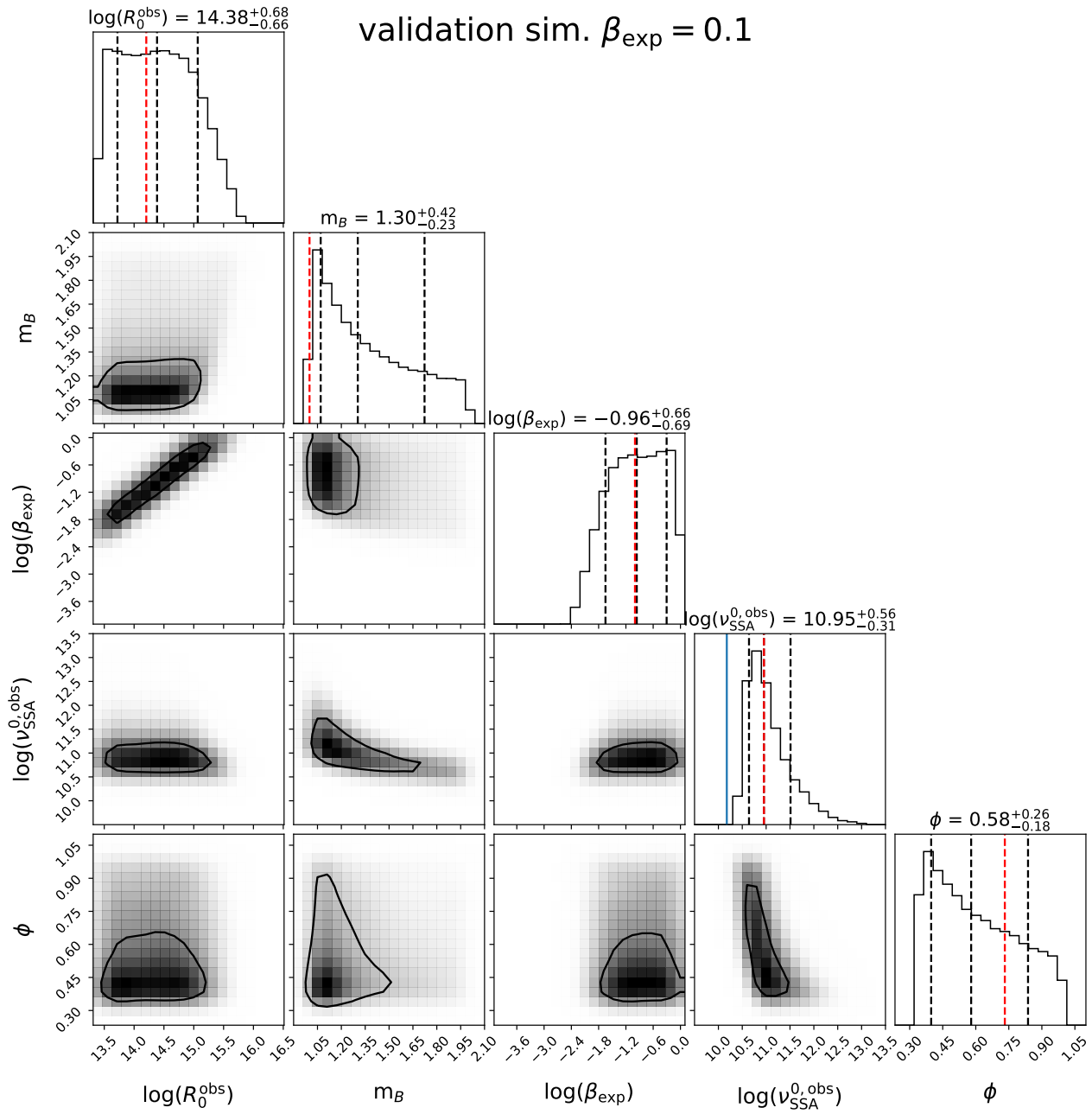


Fig. C.1: MCMC sampling for the validation of the analysis presented in Section 7. The validation is performed against the simulations for  $\beta_{\text{exp}} = 0.1$ . The vertical red dashed lines indicate the input values from the simulation.

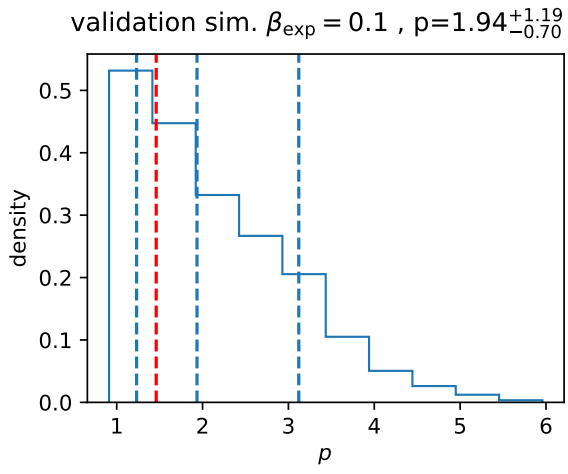


Fig. C.2: Same as in Figure 19, but for the  $p$  index regarding the MCMC validation reproduced in Figure C.2. The vertical red dashed line indicates the input value of  $p$  for the simulation.